

**Angular Distribution Models for Top-of-Atmosphere Radiative Flux
Estimation from the Clouds and the Earth's Radiant Energy System
Instrument on the Tropical Rainfall Measuring Mission Satellite.**

Part II: Validation

Norman G. Loeb¹

Center for Atmospheric Sciences, Hampton University, Hampton, Virginia

Konstantin Loukachine

Science Applications International Corporation, Hampton, Virginia

Natividad Manalo-Smith

Analytical Services and Materials, Inc., Hampton, Virginia

Bruce A. Wielicki and David F. Young

NASA Langley Research Center, Hampton, Virginia

Journal of Applied Meteorology

Submitted December, 2002

¹ *Corresponding Author Address:* Dr. Norman G. Loeb, Mail Stop 420, NASA Langley Research Center, Hampton, VA 23681-2199, U.S.A.

Abstract

Top-of-atmosphere (TOA) radiative fluxes from the Clouds and the Earth's Radiant Energy System (CERES) are estimated by applying empirical Angular Distribution Models (ADMs) that convert instantaneous radiance measurements to TOA fluxes. This paper evaluates the accuracy of CERES TOA fluxes from a new set of ADMs developed for the CERES instrument on board the Tropical Rainfall Measuring Mission (TRMM). The uncertainty in regional monthly mean reflected shortwave (SW) and emitted longwave (LW) TOA fluxes are less than 0.5 W m^{-2} based on comparisons with TOA fluxes evaluated by direct integration of the measured radiances. When stratified by viewing geometry, TOA fluxes from different angles are consistent to within 2% in the SW, and 0.7% (or 2 W m^{-2}) in the LW. In contrast, TOA fluxes based on ADMs from the Earth Radiation Budget Experiment (ERBE) applied to the same CERES radiance measurements show a 10% relative increase with viewing zenith angle in the SW, and a 3.5% (9 W m^{-2}) decrease with viewing zenith angle in the LW. Based on multiangle CERES radiance measurements, regional instantaneous TOA flux errors from the new CERES ADMs are estimated to be $< 10 \text{ W m}^{-2}$ in the SW, and $< 3.5 \text{ W m}^{-2}$ in the LW. The errors show little or no dependence on cloud phase, cloud optical depth and cloud infrared emissivity. An analysis of cloud radiative forcing (CRF) sensitivity to differences between ERBE and CERES/TRMM ADMs, scene identification and directional models shows that ADM and clear-sky scene identification differences can lead to CRF root-mean-square (RMS) differences of 8 W m^{-2} in the SW, and 4 W m^{-2} in the LW. Monthly mean SW and LW CRF differences can reach 3 W m^{-2} . In contrast, CRF is found to be insensitive to differences between ERBE and CERES/TRMM directional models.

1. Introduction

The Clouds and the Earth's Radiant Energy System (CERES) investigates the critical role that clouds and aerosols play in modulating the radiative energy flow within the Earth-atmosphere system (Wielicki et al., 1995). CERES builds upon the foundation laid by previous missions such as the Earth Radiation Budget Experiment (ERBE) (Barkstrom, 1984) to provide accurate top-of-atmosphere (TOA) radiative fluxes together with coincident cloud and aerosol properties inferred from high-resolution imager measurements.

The CERES instrument measures radiances in three channels: a shortwave channel to measure reflected sunlight, a window channel to measure Earth-emitted thermal radiation in the 8-12 μm "window" region, and a total channel to measure wavelengths between 0.3 and 200 μm . After removing the influence of instrument spectral response from the measurements (Loeb et al., 2001), CERES radiances are converted to reflected shortwave (SW), emitted longwave (LW) and emitted window (WN) TOA radiative fluxes. The radiance-to-flux conversion involves applying scene-dependent empirical Angular Distribution Models (ADMs) constructed from several months of CERES data. In Part I of this study, Loeb et al. (2002) provided a detailed description of the methodology used to construct the CERES/TRMM ADMs. The objective of this paper is to estimate the accuracy of TOA fluxes generated from the new CERES/TRMM ADMs. This involves detailed comparisons between regional ADM-derived TOA fluxes and TOA fluxes evaluated by direct integration of the measured radiances, self-consistency tests to examine whether the ADM-derived TOA fluxes show any systematic dependence upon satellite viewing geometry, and the use of multiangle CERES measurements to test the self-consistency of instantaneous TOA fluxes over the same scene. In order to compare the results with ERBE, the same set of consistency tests are also performed using TOA fluxes from the CERES "ERBE-

like” product, which uses ERBE ADMs to derive TOA fluxes from CERES measurements. A separate analysis is also performed to examine the sensitivity in regional cloud radiative forcing to changes in ADMs, scene identification and directional model differences for two regions in the west and east Pacific Ocean.

2. Observations

CERES/TRMM was launched on November 27, 1997 in a 350-km circular, precessing orbit with a 35° inclination angle. TRMM has a 46-day repeat cycle, so that a full range of solar zenith angles over a region are acquired every 46 days. On TRMM, CERES has a spatial resolution of approximately 10 km (equivalent diameter) and operates in three scan modes: crosstrack, alongtrack, and rotating azimuth plane (RAP) mode. In RAP mode, the instrument scans in elevation as it rotates in azimuth, thus acquiring radiance measurements from a wide range of viewing configurations. The CERES instrument on TRMM was shown to provide an unprecedented level of calibration stability ($\approx 0.25\%$) between in-orbit and ground calibration (Priestley et al., 1999). Unfortunately, the CERES/TRMM instrument suffered a voltage converter anomaly and acquired only 9 months of scientific data.

All nine months of the CERES/TRMM Single Scanner Footprint TOA/Surface Fluxes and Clouds (SSF) product between 38°S-38°N from January-August 1998, and March 2000, are considered. The CERES SSF product combines CERES radiances and fluxes with scene identification information inferred from coincident high spatial and spectral resolution Visible Infrared Scanner (VIRS) measurements (Kummerow et al., 1998), and meteorological fields based on European Centre for Medium-Range Weather Forecasts (ECMWF) data assimilation analysis (Rabier et al, 1998). A comprehensive description of all parameters appearing in the CERES SSF is provided in the CERES Collection Guide (Geier et al., 2001). During the 9

months of CERES data acquisition, CERES was in a crosstrack scan mode for 192 days, a RAP scan mode for 68 days, and an alongtrack scan mode for 9 days. Only CERES footprints that at least partially lie within the VIRS imager swath and whose centroids can be located on the Earth's surface are retained in the SSF product. Since VIRS scans in the crosstrack direction to a maximum viewing zenith angle of 49° , CERES footprints with viewing zenith angles $> 49^\circ$ do not appear in the SSF product when CERES is in a crosstrack scan mode. Footprints with viewing zenith angles $> 49^\circ$ are available in the SSF product only when CERES scans in either a RAP or alongtrack mode.

TOA fluxes in the SSF product are compared with TOA fluxes in the CERES “ERBE-like” product on a footprint-by-footprint basis. The CERES ERBE-like product is produced in order to extend the historical record of Earth radiation budget observations by processing CERES measurements with algorithms developed during ERBE (Smith et al., 1986). Note that since the ERBE-like product is produced independently of VIRS, all CERES FOVs (including those outside of the VIRS swath) are retained in this product. However, in order to compare TOA fluxes from the ERBE-like and SSF products, only CERES FOVs common to both are considered in this study.

3. Results

3.1 TOA Flux Consistency with Viewing Geometry

One approach for identifying potential biases in the radiance-to-flux conversion is to examine whether large ensemble averages of all-sky ADM-derived TOA fluxes exhibit any dependence upon viewing geometry. For a given solar zenith angle, average all-sky TOA fluxes should be independent of satellite viewing geometry since TOA flux is not a function of observation angle. This test has previously been used by Payette (1989) and Suttles et al. (1992)

with ERBE TOA SW and LW fluxes. They found a 10% relative increase in ERBE TOA albedo with increasing viewing zenith angle, and a 6-7% relative decrease in LW TOA flux with increasing viewing zenith angle. Loeb et al. (2000) performed a similar analysis using ADMs determined from POLDER measurements for scene types defined as a function of POLDER-based cloud property retrievals. In that analysis, albedos showed a much smaller dependence on viewing geometry than the earlier ERBE results.

Figs. 1a-b show 9-month average all-sky ERBE-like and SSF TOA albedos stratified by viewing zenith angle and relative azimuth angle for solar zenith angles (θ_0) between 40° and 50° . The gray line corresponds to the albedo determined by direct integration of the measurements. The direct integration albedo is determined by sorting CERES radiances for the entire tropics into discrete angular bins defined by the sun-earth-satellite viewing geometry, averaging the radiances in each angular bin, and integrating the radiances over all angles to produce a TOA flux (Eq. 4 in Loeb et al., 2002). A TOA albedo is obtained by normalizing the TOA flux by the incident solar irradiance. Since the direct integration method determines TOA albedo directly from measurements without the need for scene identification or angular modeling, it provides powerful check on the accuracy of average ADM-derived TOA albedos.

The ERBE-like albedos (Fig. 1a) show a systematic relative increase of 10% from nadir to the limb, consistent with the earlier results of Payette (1989) and Suttles et al. (1992). TOA albedos are underestimated close to nadir, and overestimated at large viewing zenith angles. In contrast, CERES SSF albedos show little dependence on viewing geometry and generally remain within a few percent of the albedo determined by direct integration. Similar results are obtained at other solar zenith angles (not shown).

In the LW, both the CERES SSF and ERBE-like all-sky TOA fluxes decrease with viewing zenith angle (Fig. 2). The ERBE-like all-sky TOA flux decreases by 3.5% (or 9 W m^{-2}), compared to 0.7% ($< 2 \text{ W m}^{-2}$) for the SSF TOA flux. Since CERES SSF WN ADMs are based on the same scene type stratification as the LW ADMs, TOA WN fluxes show a similar dependence on viewing zenith angle as in the LW. Note that since the ERBE-like product does not provide TOA WN fluxes, only CERES SSF WN fluxes are shown in Figs. 2c-d.

3.2 Regional Mean TOA Flux Comparison with Direct Integration

The three main sources of error in gridded time-averaged TOA fluxes are calibration, angular sampling (radiance-to-flux conversion) and time sampling. Based on several previous studies of Nimbus-7 and ERBE data, and improvements in CERES measurement strategy, Wielicki et al. (1995) predicted that the overall error in CERES monthly regional TOA flux would be 2.5 W m^{-2} in the SW and $\approx 2 \text{ W m}^{-2}$ in the LW. They estimated that calibration uncertainty would account for $\approx 1 \text{ W m}^{-2}$, angular sampling would account for $0.5\text{-}1.0 \text{ W m}^{-2}$, and temporal sampling would account for $1\text{-}2 \text{ W m}^{-2}$.

In order to isolate the angular sampling or ADM error contribution, we compare ADM-derived all-sky TOA fluxes with TOA fluxes obtained by direct integration of the measured radiances on a region-by-region basis. TOA fluxes from the direct integration method are obtained in the same manner as in Section 3.1, but for specific regions rather than for the entire tropics. Because only 9 months of CERES/TRMM crosstrack, RAP and alongtrack measurements are available, and because the direct integration approach requires CERES radiances over a wide range of solar zenith angle, viewing zenith angle and relative azimuth angle, the regions must be large enough to ensure adequate sampling in each angular bin. Based on sensitivity tests, region sizes of $20^\circ \times 20^\circ$ latitude-longitude in the SW, and $10^\circ \times 10^\circ$ latitude-

longitude regions in the LW were found to provide adequate sampling over most CERES/TRMM angular bins. In angular bins where measurements are missing, the strategy for filling in angular bins described in Section 4 of Loeb et al. (2002) is used.

To determine the regional mean ADM-derived TOA fluxes, instantaneous TOA flux estimates are first averaged into discrete angular bins in each region. Next, the difference between ADM and direct integration TOA fluxes are determined from the following:

$$\Delta F^{SW}(\theta_{oi}; \Theta_p, \Phi_q) = \frac{1}{n_l} \frac{1}{n_k} \sum_{l=1}^{n_l} \sum_{k=1}^{n_k} (\bar{F}_{ADM}^{SW}(\theta_{oi}, \theta_k, \phi_l; \Theta_p, \Phi_q) - F_{DI}^{SW}(\theta_{oi}; \Theta_p, \Phi_q)) \chi_k \quad (1)$$

$$\Delta F^{LW}(\Theta_p, \Phi_q) = \frac{1}{n_k} \sum_{k=1}^{n_k} (\bar{F}_{ADM}^{LW}(\theta_k; \Theta_p, \Phi_q) - F_{DI}^{LW}(\Theta_p, \Phi_q)) \chi_k \quad (2)$$

where $\bar{F}_{ADM}^{SW}(\theta_{oi}, \theta_k, \phi_l; \Theta_p, \Phi_q)$ and $\bar{F}_{ADM}^{LW}(\theta_k; \Theta_p, \Phi_q)$ are the mean SW and LW ADM-derived TOA fluxes for latitude-longitude region (Θ_p, Φ_q) , $F_{DI}^{SW}(\theta_{oi}; \Theta_p, \Phi_q)$ and $F_{DI}^{LW}(\Theta_p, \Phi_q)$ are the SW and LW direct integration TOA fluxes, n_k and n_l are the number of relative azimuth and viewing zenith angle bins, respectively. χ_k is a normalized weighting factor that accounts for the viewing zenith angle sampling over a 1° grid-box. χ_k is derived from the distribution of daily grid-average viewing zenith angles for 1 month of crosstrack CERES ERBE-like measurements (Fig. 3). As shown in Fig. 3, the largest relative contribution occurs at viewing zenith angles near 70° .

Since the TRMM spacecraft is in a precessing orbit with a 46-day repeat cycle, each solar zenith angle bin θ_{oi} in Eq. (1) is sampled in every region at least five times over the 9 months of CERES/TRMM measurements. To estimate the monthly regional SW TOA flux bias, $\Delta F^{SW}(\theta_{oi}; \Theta_p, \Phi_q)$ values from each region are temporally averaged over one month as follows:

$$\Delta F^{SW}(\Theta_p, \Phi_q) = \frac{1}{n_d} \frac{1}{n_t} \sum_{l=1}^{n_d} \sum_{k=1}^{n_t} \Delta F^{SW}(\theta_{oi}^k; \Theta_p, \Phi_q) \quad (3)$$

where n_d is the number of days in a month, n_t is the number of time-steps used to determine a 24-hour average flux bias, and θ_{oi}^k is the midpoint of the CERES solar zenith angle bin corresponding to the solar zenith angle at time-step k . To evaluate Eq. (3), the solar zenith angle sampling for the month of March 1998 is used with 144 ten-minute time-steps.

Regional SW TOA flux bias errors are shown in Figs. 4a-d and summarized in Table 1 for both CERES ERBE-like and SSF TOA fluxes. Separate analyses are performed for two viewing zenith angle ranges: nadir to 50°, and nadir to 70°. In the CERES/TRMM SSF product, CERES footprints are retained only when they at least partially lie within the VIRS imager swath, which has a maximum viewing zenith angle of 49°. Therefore, the 50° viewing zenith angle cut-off is representative of the angular sampling when CERES is in a crosstrack scan mode, and the 70° cut-off is representative of angular sampling in the SSF product when CERES is in a RAP scan mode (radiance-to-flux conversion is not performed when $\theta > 70^\circ$). In RAP mode, CERES footprints at viewing zenith angles $> 49^\circ$ appear on the SSF when the angle between the CERES scan plane and the satellite orbital plane is less than 90°.

Over most of the Tropics, the ERBE-like SW TOA fluxes for the nadir to 50° viewing zenith angle range (Fig. 4a) are smaller than SW TOA fluxes evaluated by direct integration. The average TOA flux bias error is -2.7 W m^{-2} . In contrast, both positive and negative bias errors are observed for the CERES SSF SW TOA fluxes (Fig. 4b), and the bias over the entire Tropics is close to zero. The root-mean-square (RMS) error in the SSF regional mean SW TOA flux is 1.4 W m^{-2} , which is larger than the $0.5\text{-}1.0 \text{ W m}^{-2}$ error predicted by Wielicki et al. (1995). When

viewing zenith angles from nadir to 70° are considered, the ERBE-like SW TOA flux bias error (Figs. 4c) is 0.43 W m^{-2} . This reduction in bias error is due to error compensation at large and small viewing zenith angles. The CERES SSF SW TOA flux bias error (Fig. 4d) remains close to zero and the RMS error in the regional mean TOA flux is now 0.51 W m^{-2} , which is well within the range predicted by Wielicki et al. (1995).

In the LW, the ERBE-like product overestimates LW TOA fluxes for viewing zenith angles between nadir and 50° (Fig. 5a). The average LW flux bias is 4.4 W m^{-2} , compared to 0.87 W m^{-2} for the SSF (Fig. 5b). For viewing zenith angles between nadir and 70° , the ERBE-like TOA flux bias is 1.2 W m^{-2} (Fig. 5c), compared to 0.29 W m^{-2} for SSF. The RMS error in the SSF regional mean LW TOA flux for viewing zenith angles $< 70^\circ$ is 0.49 W m^{-2} , which is also within the 0.5 W m^{-2} accuracy predicted by Wielicki et al. (1995).

3.3 Regional Instantaneous TOA Flux Consistency Test

Because scanning radiometers can only measure TOA radiances from a limited number of directions over a scene at any one time, it is not possible to use an approach like the direct integration method to validate instantaneous ADM-derived TOA fluxes. However, since the actual TOA flux is independent of satellite viewing geometry, a powerful consistency check is to compare instantaneous TOA fluxes estimated from multiangle measurements over the same scene. If the TOA flux estimates from different angles are not the same, this indicates that the anisotropy of the scene is poorly characterized by the ADM. Conversely, if the TOA flux estimates are the same, this provides some confidence that the anisotropy of the scene is modeled correctly. Note, however, that “consistency” is not a guarantee of absolute accuracy since it does not account for potential bias errors that are independent of viewing geometry.

To examine the consistency of ADM-derived TOA fluxes, multiangle CERES/TRMM measurements from 9 alongtrack days are considered. When CERES scans in the alongtrack scan mode, it acquires measurements from limb-to-limb along the satellite groundtrack. The VIRS imager observes the same area as CERES within approximately 2 minutes, but from viewing zenith angles close to nadir (Fig. 6). In order to take advantage of the close VIRS/CERES spatial and temporal coincidence, instantaneous TOA fluxes from CERES are averaged over 1° latitude-longitude regions and are compared with broadband TOA fluxes estimated from colocated VIRS narrowband (nadir) radiances. A VIRS footprint-average $0.63\text{-}\mu\text{m}$ radiance is converted to a broadband radiance by applying a narrow-to-broadband correction derived from a linear fit between all coincident nadir CERES and VIRS footprint-average $0.63\text{-}\mu\text{m}$ radiances that lie within the appropriate 1° latitude-longitude region. The VIRS broadband radiances are then converted to TOA fluxes in the same manner as CERES radiances (Loeb et al. 2002). To optimize spatial matching between CERES and VIRS measurements, VIRS pixels within CERES FOVs have been weighted by the CERES Point Spread Function (PSF) (Smith, 1994). Consequently, the main error sources in the comparison are ADM errors and narrow-to-broadband conversion errors. Based on a separate analysis of TOA fluxes from the two CERES instruments on the Terra spacecraft, the relative error in TOA flux introduced by the narrow-to-broadband conversion is estimated to be 1.61% in the SW and 1.54% in the LW.

Figs. 7a-d show the consistency between TOA fluxes from VIRS nadir and CERES off-nadir radiance measurements. All-sky results are based upon 13,259 1° -regions, and results for cloud-free conditions (as identified from VIRS) are based upon 1,701 1° -regions. TOA flux consistency is measured by the RMS difference between VIRS and CERES TOA fluxes. In all cases, TOA flux differences increase with increasing CERES and VIRS viewing zenith angle

difference. This increase is more pronounced in the ERBE-like results. When the VIRS and CERES viewing zenith angle separation is between 60° and 70° , the relative RMS difference (defined as the VIRS-CERES TOA flux RMS difference divided by the mean TOA flux) in all-sky SW TOA flux is a factor of 2.2 smaller for the SSF than it is for ERBE-like. In the LW, the SSF relative RMS difference is reduced by a factor of 1.55 compared to ERBE. Under cloud-free conditions the SSF relative RMS differences are smaller by factors 1.45 and 1.55 in the SW and LW, respectively.

Because the true instantaneous TOA flux for a CERES FOV is unavailable, there is no direct way of determining the actual instantaneous TOA flux error. Since TOA flux consistency and TOA flux error are likely closely related, however, it is possible to provide an indirect estimate of TOA flux error. To determine the relationship between TOA flux “consistency” and “true” flux error, ADMs are applied to radiances and fluxes generated from a broadband radiative transfer model. For each scene, the TOA flux consistency between nadir and off-nadir viewing zenith angles is compared with the actual TOA flux error. Based on simulations involving the radiative transfer model of Nakajima and Tanaka (1986) for clouds with optical depths between 0.1 and 200, the TOA flux error is found to be linearly proportional to the TOA flux consistency. In fact, when ADM-derived TOA fluxes at nadir and $\theta=65^\circ$ are compared, the RMS error is approximately half as large as the RMS difference. Table 2 provides estimates of TOA flux errors corresponding to the results in Fig. 7 using this approximation. To be consistent with Wielicki et al. (1995), the SW TOA flux errors are defined for a TOA solar irradiance of 1000 W m^{-2} (i.e., a solar zenith angle of 42.895°). SSF all-sky SW and LW TOA flux errors are 9.8 and 3.5 W m^{-2} , respectively. These are well below the CERES goals set by Wielicki et al. (1995). Note that the ERBE-like all-sky TOA flux error of 22 W m^{-2} differs from the 37.5 W m^{-2}

provided in Table 4 of Wielicki et al. (1995) because the Wielicki et al. (1995) value corresponds to TOA flux consistency rather than TOA flux error.

Figs. 8a-d show TOA flux errors as a function of cloud optical depth and cloud infrared emissivity for liquid water and ice clouds. In the SW, SSF TOA flux errors are generally less than 20 W m^{-2} , and show little dependence on cloud optical depth. In contrast, ERBE-like TOA flux errors are a factor of 2-5 larger (reaching 65 W m^{-2}), and depend strongly on cloud optical depth. The largest improvement in TOA flux accuracy from the SSF ADMs occurs for thin ice clouds and thick liquid water clouds. In the LW, SSF TOA flux errors are generally a factor of 1.5-2.0 smaller than ERBE-like. The largest errors in both SSF and ERBE-like TOA fluxes occur for cloud infrared emissivities between 0.5 and 0.7, where SSF TOA flux errors reach 6 W m^{-2} and ERBE-like TOA flux errors reach 13 W m^{-2} .

3.4 CERES SSF and ERBE-like TOA Flux Differences By Cloud Type

One of the advances of the new CERES/TRMM SSF ADMs over ERBE is improved sensitivity to parameters that influence the anisotropy of the observed scenes. To examine the difference between CERES SSF and ERBE-like instantaneous TOA fluxes, Figs. 9-10 show SW (for $\theta_o=42^\circ\text{-}44^\circ$) and LW TOA flux differences (ERBE-like minus SSF) stratified by cloud phase, cloud optical depth and cloud infrared emissivity. Because ERBE-like SW ADMs underestimate (overestimate) the anisotropy of thin (thick) clouds (Loeb et al., 2002), SW TOA flux differences for $\theta < 25^\circ$ (Figs. 9a and 9c) are negative for thin clouds, and positive for thick clouds. When all viewing zenith angles are considered (Figs. 9b and 9d), TOA flux differences show a broader distribution because differences in anisotropy between ERBE and SSF ADMs depend on viewing zenith angle (c.f., Fig. 13 of Loeb et al., 2002). In the LW (Fig. 10), TOA flux differences are smaller, but nonetheless depend systematically on cloud infrared emissivity.

3.5 Cloud Radiative Forcing Sensitivity to ADMs, Scene Identification and Directional Models

For climate studies there often is a need to compare the radiative effects of clouds between different regions or over the same region during different time periods. A metric commonly used to assess the radiative impact of clouds on the climate system is cloud radiative forcing (CRF) (Ramanathan et al., 1989; Harrison et al., 1990), which is defined as the TOA flux difference between clear and all-sky conditions. To examine how differences between ERBE and SSF ADMs affect regional CRF, we consider two regions with distinct cloud properties, namely, the west (5°S-5°N, 140°E-165°E) and east (5°S-5°N, 80°W-105°W) tropical Pacific Ocean. Because of their sensitivity to El Niño-Southern Oscillation (ENSO) events, these regions have received a great deal of attention recently (e.g. Wong et al., 2000; Cess et al., 2001; Lindzen et al., 2001; Lin et al., 2002; Chambers et al., 2002). During a non-El Niño year, the west Pacific Ocean region (or warm pool) is dominated by convective clouds, whereas stratiform clouds persist in the east Pacific Ocean region.

To determine the cloud radiative forcing in these two regions, daily average clear and all-sky TOA fluxes are inferred from instantaneous SW and LW TOA fluxes and averaged into 1° latitude-longitude regions. An instantaneous TOA flux is converted to a daily mean TOA flux by modeling the diurnal variation of albedo using scene-type dependent directional albedo models (Brooks et al., 1986; Young et al., 1998) derived from the CERES/TRMM ADMs. In order to isolate the influence of ERBE and SSF ADM differences on CRF, the same population of clear scenes (as identified by VIRS) is used to determine both ERBE-like and SSF CRF, and the same directional models (i.e., derived from the CERES/TRMM ADMs) are used in both cases to derive daily mean TOA fluxes.

Figs. 11a-f compare cloud properties and SW CRF differences between CERES ERBE-like and SSF for the two regions in March 2000. During the entire month, the CERES instrument was in a crosstrack scan mode. As a result, only CERES footprints with viewing zenith angles less than 49° are available for this period in the SSF product. Therefore, these results provide an upper bound on CRF sensitivity to differences between the ERBE and CERES SSF ADMs. SW CRF differences (ERBE-like minus SSF) are generally larger in the west Pacific Ocean region, as is evident from the broader frequency distributions in Fig. 11e compared to Fig. 11f. A positive (negative) SW CRF difference means the ERBE ADMs produce less (more) SW radiative cooling than the SSF ADMs. Results in Figs. 11c-d suggest that ERBE-like ADMs produce less SW radiative cooling for thin clouds, and more SW radiative cooling for thick clouds as compared to CERES SSF ADMs. For ice clouds, SW CRF differences range from $+10 \text{ W m}^{-2}$ for clouds of optical depth near 2, to -15 W m^{-2} for clouds with optical depths > 35 . SW CRF differences are smallest ($< 2 \text{ W m}^{-2}$) for liquid water clouds with optical depths < 5 . Overall, ERBE ADMs produce 2.6 W m^{-2} (5.3%) less SW radiative cooling than SSF ADMs in the west Pacific Ocean region (Table 3), and 0.3 W m^{-2} (0.7%) more SW radiative cooling in the east Pacific Ocean region (Table 4). The RMS difference in 1° daily mean SW CRF is $7 - 8 \text{ W m}^{-2}$ (15%).

LW CRF differences between CERES and ERBE-like are shown in Figs. 12a-f as a function of cloud infrared emissivity. A positive (negative) LW CRF difference means the ERBE ADMs produce more (less) LW radiative warming than the SSF ADMs. For most cloud conditions, the ERBE-like ADMs produce less LW radiative warming. This is not unexpected given the large positive bias errors in ERBE-like LW TOA fluxes in Fig. 2a-b for viewing zenith angles $< 50^\circ$. Differences are more pronounced for ice clouds, reaching -6 W m^{-2} at cloud

infrared emissivities between 0.1 and 0.2 in the west Pacific Ocean region (Fig. 12c). In contrast, the largest LW CRF difference in the east Pacific Ocean region occur at cloud infrared emissivities near 0.6, and decrease in magnitude with decreasing cloud infrared emissivity (Fig. 12d). This regional difference is explained by the fact that when clouds with small cloud infrared emissivity occur in the east Pacific Ocean region, their cloud fraction is generally much smaller than in the west Pacific region. This is illustrated in Figs. 13c which shows the cloud fraction distribution for clouds with cloud infrared emissivity less than 0.5. Since LW CRF decreases with decreasing cloud cover (i.e., scenes become clearer), LW CRF sensitivity to ADM differences is reduced (Figs. 13a-b). Overall, ERBE ADMs produce $\approx 2.6 \text{ W m}^{-2}$ (6.2%) less LW radiative warming in the west compared to SSF (Table 3), and $\approx 1.5 \text{ W m}^{-2}$ (6.3%) less LW radiative warming in the east (Table 4). RMS differences in 1° daily mean LW CRF for the two regions ranges from $2.5 - 4 \text{ W m}^{-2}$ (10%).

Since SW and LW CRF differences in the west Pacific Ocean region have approximately the same magnitude but opposite sign, the difference in net CRF between CERES ERBE-like and SSF is only 0.1 W m^{-2} (1.4%) (Table 3), whereas ERBE-like predicts a net cooling in the east that is 1.7 W m^{-2} (8%) larger than SSF.

The above results demonstrate how differences between ERBE-like and SSF ADMs alone affect CRF. In practice, however, differences in scene identification and temporal sampling can also be important. Scene identification for ERBE is determined from the Maximum Likelihood Estimation (MLE) technique (Wielicki and Green, 1989) which uses SW and LW radiances to classify a scene as either clear, partly cloudy, mostly cloudy or overcast. ERBE temporal sampling uses directional models defined for the same scene types. The CRF sensitivity to all three factors is determined by reprocessing the data for the model combinations provided in

Table 5. Results (Fig. 14) show that while CRF is quite sensitive to changes in both ADMs and clear-sky scene identification, it has a weak dependence on what directional model is used. In the SW, clear scenes identified by the ERBE MLE are brighter by 1 to 2 W m^{-2} due to undetected boundary layer cloud contamination. In the LW, clear scenes from the ERBE MLE produce TOA fluxes that are 1.4 W m^{-2} larger in the east Pacific Ocean region and 0.3 W m^{-2} smaller in the west. Net CRF sensitivity to clear-sky scene identification is between 1.8 to 3 W m^{-2} . These differences are smaller than those in a recent paper by Stubenrauch et al. (2002) who compared TOA fluxes for clear scenes identified from ERBE and ISCCP. In that study, SW TOA fluxes for ERBE clear scenes are actually smaller than ISCCP by 5-10 W m^{-2} , and clear-sky LW TOA fluxes are larger by 4 W m^{-2} .

The official CERES products that provide monthly average regional TOA fluxes and CRF results are the CERES Monthly TOA/Surface Averages (SRBAVG) and ERBE-like Monthly Geographic Averages (ES4) products. The CERES SRBAVG product consists of monthly 1° regional mean TOA fluxes derived from CERES SSF instantaneous TOA fluxes. The non-GEO version uses directional models based on the SSF ADMs, and the GEO version merges CERES measurements with geostationary satellite measurements to more accurately resolve the diurnal variation in TOA fluxes (Young et al., 1998). The CERES ES-4 product consists of monthly mean 2.5° regional mean TOA fluxes derived from ERBE-like instantaneous TOA fluxes and the ERBE directional models (Wong et al., 2000). Tables 6 and 7 show TOA flux and CRF results for the west and east Pacific Ocean regions during March 1998 and March 2000, respectively. The dramatic difference in TOA fluxes and CRF between these two months is due to the strong ENSO event that occurred in early 1998. While ES4, Non-Geo and GEO results are generally consistent to within 3 W m^{-2} , differences are larger in the eastern Pacific Ocean region

in March 1998. For that month, ES4 SW radiative cooling is larger by approximately 6.5 W m^{-2} and LW radiative warming is larger by 5 W m^{-2} . One explanation for the larger difference may be related to the dramatic increase in convection in the eastern Pacific Ocean region in March 1998 compared to normal years. Based on ADM differences alone, an increase in cloud optical depth produces larger ERBE-like SW TOA fluxes (c.f., Figs. 9). In the LW, most of the discrepancy (3.4 W m^{-2}) is explained by clear-sky LW TOA flux differences. Another factor that may affect the results is the difference in sampling between the ES-4 and SRBABVG products. Because the ES-4 product does not rely on information from VIRS, it is based on instantaneous TOA fluxes over the entire CERES swath and thus uses approximately twice the number of measurements as the SBAVG product. If the clouds sampled in the ES-4 product for that month happened to be dramatically different from those sampled by the SRBABVG product, this could also cause larger differences.

4. Discussion

Results in the preceding sections clearly demonstrate the improvement in TOA flux accuracy from the CERES SSF product. This improvement is mainly due to an increase in the number of ADM scene types and improved scene identification from the VIRS imager. It should be noted, however, that since the VIRS scene identification relies on several assumptions to both detect clouds and infer their optical properties, larger instantaneous TOA flux errors are expected in certain conditions. These include multi-layer cloud conditions, where conventional passive remote sensing threshold techniques often fail to even identify more than one cloud layer (Baum and Spinhirne, 2000), in the presence of vertically extensive clouds, where 3D effects such as cloud shadows and enhanced cloud-side illumination can result in anisotropic patterns that deviate significantly from average conditions, and in regions where topographical variations are

pronounced. Such conditions likely play a key role in explaining systematic angle-dependent biases in observed large-ensemble averages of cloud fraction (Minnis, 1989), cloud optical depth retrievals (Loeb and Davies, 1996; Loeb and Coakley, 1998) and LW surface anisotropy (Minnis and Khaiyer, 2000). Another situation where instantaneous TOA flux errors are likely to be larger is in sunglint over water surfaces, which can occur in clear, broken and thin overcast cloud conditions. In sunglint the anisotropy changes very rapidly with observation angle. The relatively coarse angular bins used to define CERES ADMs cannot resolve such variability.

A more subtle effect that has yet to be quantified is the influence of CERES FOV growth with viewing zenith angle on ADM-derived TOA fluxes. The equivalent circle diameter of a CERES/TRMM footprint increases from 10 km at nadir to 45 km at $\theta=70^\circ$, and reaches 95 km at $\theta=80^\circ$. Because ADMs are constructed by compositing CERES radiances for the same “scene type” in every angular bin, the anisotropy of a given scene type is thus determined from FOVs whose spatial resolution varies by at least an order of magnitude. Ye and Coakley (1996) demonstrated that FOV growth with viewing zenith angle has a significant effect on the ERBE scene identification. More study is needed to quantify how this affects TOA fluxes from ADMs based on imager scene identification.

It should also be pointed out that because cloud properties depend on cloud size, cloud populations defined for a given set of criteria at nadir may be very different from those defined for the same criteria at oblique viewing zenith angles. As an example, Fig. 15a-b show TOA albedo, cloud optical depth, LW TOA flux and cloud-top temperature against CERES viewing zenith angle for overcast scenes from 9 alongtrack days. Albedo increases with viewing zenith angle from 0.416 to 0.458, and LW flux decreases from 211.8 W m^{-2} to 195.3 W m^{-2} . These large changes in albedo and LW flux with viewing zenith angle are not due to ADM errors, but rather

to changes in the physical properties of overcast clouds with FOV size. This is clearly evident from the imager-derived cloud optical depth and cloud-top temperature curves in Figs. 15a-b. When CERES is in the alongtrack scan mode, the imager observes CERES FOVs from near-nadir viewing zenith angles. Therefore, from the imager vantage point, an increase in CERES viewing zenith angle corresponds only to an increase in size of the overcast scene. As the horizontal extent of the clouds increases, results in Figs. 15a-b show that clouds become thicker and colder. One method of reducing this dependence on FOV size is to use more parameters to define the scene type. For example, by defining the cloud population for discrete intervals of cloud fraction, optical depth, phase etc., the cloud population will have similar physical properties over a wide range spatial scales. Note that while the physical properties of the clouds will be less sensitive to FOV size, their frequency-of-occurrence will still depend strongly on FOV size.

5. Summary

The CERES/TRMM Single Scanner Footprint SSF product provides broadband TOA radiative fluxes over the tropics in the SW, LW and WN regions together with coincident imager-derived cloud and aerosol properties, and atmospheric state parameters from 4-D assimilation products. One of the major advances in CERES is the availability of improved ADMs for estimating TOA radiative fluxes from broadband radiance measurements. Multiangle CERES measurements and coincident imager cloud information are used to construct empirical ADMs for scene types defined by parameters that have a strong influence on the anisotropy (or angular dependence) of TOA radiances. The CERES/TRMM ADMs are available for viewing and downloading at the following web address: <http://asd-www.larc.nasa.gov/Inversion/>.

The advantages of combining CERES and imager data are demonstrated by comparing TOA fluxes between the CERES SSF and ERBE-like products. The CERES SSF product uses the new CERES ADMs, whereas fluxes on the ERBE-like product are based on ADMs developed during the ERBE experiment for only 12 scene types. When stratified by sun-Earth-satellite viewing geometry, all-sky mean TOA fluxes from the new CERES ADMs are consistent to within 2% in the SW, and 0.7% (or 2 W m^{-2}) in the LW. In contrast, ERBE-like mean fluxes show a systematic dependence on viewing zenith angle of 10% in the SW, and 3.5% (or 9 W m^{-2}) in the LW. Regional TOA flux uncertainties from the CERES SSF is shown to be $< 0.5 \text{ W m}^{-2}$ both in the SW and LW, which is within pre-launch CERES accuracy goals set by Wielicki et al. (1995). Multiangle consistency checks show that regional instantaneous TOA flux errors from the new CERES ADMs are smaller than those from the ERBE ADMs by factors of 2.2 and 1.68 in the SW and LW, respectively, for all-sky conditions. We estimate that regional instantaneous TOA fluxes are accurate to within 10 W m^{-2} in the SW, and 3.5 W m^{-2} in the LW, and show little dependence on cloud phase, cloud optical depth (SW) or infrared cloud emissivity (LW). In contrast, TOA flux errors from ERBE-like are a strong function of these parameters—ERBE-like TOA flux errors are larger than SSF errors by factors of 3-4 for thin ice clouds and 3-6 for thick liquid water and ice clouds.

Cloud radiative forcing (CRF) sensitivity to ADM differences is estimated from instantaneous ERBE-like and SSF TOA fluxes converted to 1° regional daily mean clear (according to VIRS) and all-sky TOA fluxes for two regions in the west and east Pacific Ocean. While RMS differences in CRF are typically $7 - 8 \text{ W m}^{-2}$ in the SW and $2.5 - 4 \text{ W m}^{-2}$ in the LW, differences in average CRF are typically between $0 - 3 \text{ W m}^{-2}$ in the SW and $1.5 - 2.5 \text{ W m}^{-2}$ in

the LW. These differences are comparable in magnitude to those resulting from a change in clear-sky scene identification from the ERBE MLE to the VIRS imager.

New global ADMs are currently being developed for the CERES instruments on the Terra (launched on December 18, 1999) and Aqua (launched on May 4, 2002) spacecrafts. Scene identification will take advantage of the new capabilities of the Moderate Resolution Imaging Spectroradiometer (MODIS). These ADMs will be based on at least 2 years of measurements from each instrument, which will provide enough sampling to increase the ADM angular resolution and number of scene types. As with CERES/TRMM, an extensive set of validation activities will be performed.

Acknowledgements

This research was funded by the Clouds and the Earth's Radiant Energy System (CERES) project under NASA grant NAG-1-2318. Funding was also provided from NASA grant NAG-1-01096. The authors wish to thank Drs. Takmeng Wong, Donald P. Garber and Mr. Edward A. Kizer for their help in ERBE-like and SRBAVG data analysis.

References

- Barkstrom, B.R., 1984: The Earth Radiation Budget Experiment (ERBE). *Bull. Amer. Meteorol. Soc.*, **65**, 1170-1186.
- Baum, B. A. and J. D. Spinhirne, 2000: Remote sensing of cloud properties using MODIS Airborne Simulator imagery during SUCCESS. III. Cloud overlap. *J. Geophys. Res.*, **105**, 11 793-11 804.
- Brooks, D. R., E. F. Harrison, P. Minnis, J. T. Suttles, and R. S. Kandel, 1986: Development of algorithms for understanding the temporal and spatial variability of the earth's radiation balance. *Rev. Geophys.*, **24**, 422-438.
- Cess, R.D., M. Zhang, B.A. Wielicki, D.F. Young, X.-L. Zhou, and Y. Nikitenko, 2001: The influence of the 1998 El Nino upon cloud-radiative forcing over the Pacific warm pool. *J. Climate*, **14**, 2129-2137.
- Chambers, L., L. Bing, B. A. Wielicki, Y. Hu, and K.-M. Xu, 2002: Reply. *J. Climate*, **15**, 2716-2717.
- Geier, E.B., R. N. Green, D. P. Kratz, P. Minnis, W. F. Miller, S. K. Nolan, and C. B. Franklin, 2001: Single satellite footprint TOA/surface fluxes and clouds (SSF) collection document. [available on-line from <http://asd-www.larc.nasa.gov/ceres/ASDceres.html>.]
- Harrison, E. F., P. Minnis, B. R. Barkstrom, V. Ramanathan, R. D. Cess, and G. G. Gibson, 1990: Seasonal variation of cloud radiative forcing derived from the Earth Radiation Budget Experiment. *J. Geophys. Res.*, **95**, 18 687-18 703.
- Kummerow, C., W. Barnes, T. Kozu, J. Shiue, and J. Simpson, 1998: The Tropical Rainfall Measuring Mission (TRMM) sensor package. *J. Atmos. Ocean. Tech.*, **15**, 809-817.

- Lin, B., B. A. Wielicki, L. H. Chambers, Y. Hu, and K.-M. Xu, 2002: The iris hypothesis: A negative or positive cloud feedback? *J. Climate*, **15**, 3–7.
- Lindzen, R., M.-D. Chou, and A. Hou, 2001: Does the earth have an adaptive infrared iris? *Bull. Amer. Meteor. Soc.*, **82**, 417–432.
- Loeb, N.G., and J.A. Coakley, Jr., 1998: Inference of marine stratus cloud optical depths from satellite measurements: Does 1D theory apply? *J. Climate*, **11**, 215-233.
- Loeb, N.G., and R. Davies, 1996: Observational evidence of plane parallel model biases: The apparent dependence of cloud optical depth on solar zenith angle. *J. Geophys. Res.*, **101**, 1621-1634.
- Loeb, N. G., F. Parol, J.-C. Buriez, and C. Vanbauce, 2000: Top-of-atmosphere albedo estimation from angular distribution models using scene identification from satellite cloud property retrievals. *J. Climate*, **13**, 1269-1285.
- Loeb, N. G., K. J. Priestley, D. P. Kratz, E. B. Geier, R. N. Green, B. A. Wielicki, P. O'R. Hinton, and S. K. Nolan, 2001: Determination of unfiltered radiances from the Clouds and the Earth's Radiant Energy System (CERES) instrument. *J. Appl. Meteor.*, **40**, 822-835.
- Loeb, N.G., N.M. Smith, S. Kato, W.F. Miller, S.K. Gupta, P. Minnis, and B. A. Wielicki, 2002: Angular distribution models for top-of-atmosphere radiative flux estimation from the Clouds and the Earth's Radiant Energy System instrument on the Tropical Rainfall Measuring Mission Satellite. Part I: Methodology, *J. Appl. Meteor.* (in press).
- Minnis, P., 1989: Viewing zenith angle dependence of cloudiness determined from coincident GOES East and GOES West data. *J. Geophys. Res.*, **94**, 2303-2320.

- Minnis, P., and M. M. Khaiyer, 2000: Anisotropy of land surface skin temperature derived from satellite data. *J. Appl. Meteor.*, **39**, 1117-1129.
- Nakajima, T., and M. Tanaka, 1986: Matrix formulations for the transfer of solar radiation in a plane-parallel scattering atmosphere. *J. Quant. Spectrosc. Radiat. Transfer*, **35**, 13-21.
- Payette, F., Applications of a sampling strategy for the ERBE scanner data, M.Sc. Thesis, McGill University, Montreal, Canada, 1989.
- Priestley, K. J., R. B. Lee III, R. N. Green, S. Thomas, and R.S. Wilson, 1999: Radiometric performance of the Clouds and the Earth's Radiant Energy System (CERES) proto-flight model on the Tropical Rainfall Measuring Mission (TRMM) spacecraft for 1998. *Proc. AMS 10th Conf. Atmos. Rad.*, Madison, WI, June 28-July 2, 33-36.
- Rabier, F., J.-N. Thepaut, and P. Courtier, 1998: Extended assimilation and forecast experiments with a four-dimensional variational assimilation. *Quart. J. Roy. Meteor. Soc.*, **124**, 1861-1887.
- Ramanathan, V., R. D. Cess, E. F. Harrison, P. Minnis, B. R. Barkstrom, E. Ahmad, and D. Hartmann, 1989: Cloud-radiative forcing and climate: Results from the Earth Radiation Budget Experiment. *Science*, **243**, 57-63.
- Smith, G. L., 1994: Effects of time response on the point spread function of a scanning radiometer. *Appl. Opt.*, **33**, 7031-7037.
- Smith, G. L., R. N. Green, E. Raschke, L. M. Avis, J. T. Suttles, B. A. Wielicki, and R. Davies, 1986: Inversion methods for satellite studies of the earth radiation budget: Development of algorithms for the ERBE mission. *Rev. Geophys.*, **24**, 407-421.

- Stubenrauch, C. J., V. Briand, W. B. Rossow, 2002: The role of clear-sky identification in study of cloud radiative effects: Combined analysis from ISCCP and the Scanner of Radiation Budget. *J. Appl. Meteor.*, **41**, 396-412.
- Suttles, J.T., B.A. Wielicki, and S. Vemury, 1992: Top-of-atmosphere radiative fluxes: Validation of ERBE scanner inversion algorithm using Nimbus-7 ERB data. *J. Appl. Meteor.*, **31**, 784-796.
- Wielicki, B.A., R. D. Cess, M. D. King, D. A. Randall, and E. F. Harrison, 1995: Mission to planet Earth: Role of clouds and radiation in climate. *Bull. Amer. Meteor. Soc.*, **76**, 2125-2152.
- Wielicki, B.A., and R.N. Green, 1989: Cloud identification for ERBE radiation flux retrieval. *J. Appl. Meteor.*, **28**, 1133-1146.
- Wong, T., D. F. Young, M. Haeffelin, and S. Weckmann, 2000: Validation of the CERES/TRMM ERBE-like monthly mean clear-sky longwave dataset and the effects of the 1998 ENSO event. *J. Climate*, **13**, 4256-4267.
- Ye, Q., and J.A. Coakley, Jr., Biases in Earth radiation budget observations, Part 2: Consistent scene identification and anisotropic factors. *J. Geophys. Res.*, **101**, 21 253-21 263, 1996.
- Young, D. F., P. Minnis, D. R. Doelling, G. G. Gibson, and T. Wong, 1998: Temporal interpolation methods for the Clouds and the Earth's Radiant Energy System (CERES) experiment. *J. Appl. Meteor.*, **37**, 572-590.

Figures

Figure 1 (a) ERBE-like and (b) CERES SSF mean all-sky TOA albedo for $\theta_o=40^\circ$ - 50° as a function of viewing zenith angle and relative azimuth angle.

Figure 2 All-sky mean TOA flux as a function of viewing zenith angle for (a) daytime LW; (b) nighttime LW; (c) daytime WN and (d) nighttime WN.

Figure 3 Distribution of 1° daily grid average viewing zenith angles from one month of CERES crosstrack scanning measurements.

Figure 4 Error in 1° monthly mean all-sky SW TOA flux inferred from the difference between ADM-derived TOA fluxes and TOA fluxes obtained by direct integration of measured radiances. Differences are diurnally averaged using the solar zenith angle sampling from March 1998. (a) ERBE-like for viewing zenith angles between 0° and 50° ; (b) SSF for viewing zenith angles between 0° and 50° ; (c) ERBE-like for viewing zenith angles between 0° and 70° ; (d) SSF for viewing zenith angles between 0° and 70° .

Figure 5 Error in 1° monthly mean all-sky LW TOA flux inferred from the difference between ADM-derived TOA fluxes and TOA fluxes obtained by direct integration of measured radiances. (a) ERBE-like for viewing zenith angles between 0° and 50° ; (b) SSF for viewing zenith angles between 0° and 50° ; (c) ERBE-like for viewing zenith angles between 0° and 70° ; (d) SSF for viewing zenith angles between 0° and 70° .

Figure 6 Schematic of CERES and VIRS viewing geometry for regional instantaneous TOA flux consistency tests.

Figure 7 Relative RMS difference between TOA fluxes determined from VIRS nadir radiances and off-nadir CERES measurements as a function of the viewing zenith angle separation for (a) all-sky SW TOA fluxes, (b) clear-sky SW TOA fluxes, (c) all-sky LW TOA fluxes, and (d) clear-sky LW TOA fluxes.

Figure 8 Estimated SSF and ERBE-like instantaneous SW TOA flux errors for (a) liquid water and (b) ice clouds as a function of cloud optical depth; LW TOA flux errors for (c) liquid water and (d) ice clouds as a function of cloud infrared emissivity.

Figure 9 Difference between CERES ERBE-like and CERES SSF SW TOA flux (ERBE-like minus SSF) against cloud optical depth for liquid water clouds when (a) $\theta \leq 25^\circ$, (b) $\theta \leq 70^\circ$, and for ice clouds when (c) $\theta \leq 25^\circ$ and (d) $\theta \leq 70^\circ$. The solar zenith angle range is 42° - 44° .

Figure 10 Difference between CERES ERBE-like and CERES SSF LW TOA flux (ERBE-like minus SSF) against cloud infrared emissivity for liquid water clouds when (a) $\theta \leq 25^\circ$, (b) $\theta \leq 70^\circ$, and for ice clouds when (c) $\theta \leq 25^\circ$ and (d) $\theta \leq 70^\circ$.

Figure 11 Distribution of 1° daily mean cloud optical depth (a, b), average SW CRF difference against cloud optical depth (c, d), and distribution of 1° SW CRF difference (ERBE-like minus SSF) (e, f) for the west (left column) and east (right column) Pacific Ocean regions.

Figure 12 Distribution of 1° daily mean cloud infrared emissivity (a, b), average LW CRF difference against cloud infrared emissivity (c, d), and distribution of 1° LW CRF difference (ERBE-like minus SSF) (e, f) for the west (left column) and east (right column) Pacific Ocean regions.

Figure 13 1° daily mean LW CRF difference against cloud fraction for ice clouds with cloud infrared emissivity less than 0.5 in the (a) west Pacific Ocean region and (b) east Pacific Ocean region, and (c) corresponding cloud fraction relative frequency distribution.

Figure 14 SW and LW TOA flux and CRF sensitivity to SSF and ERBE-like ADM, clear-sky scene identification and directional model differences in the (a) west Pacific Ocean region and (b) east Pacific Ocean region.

Figure 15 (a) TOA albedo ($\theta_o=40^\circ-50^\circ$) and cloud optical depth, and (b) LW TOA flux and cloud-top temperature against CERES viewing zenith angle for overcast scenes from 9 alongtrack days.

Tables

	SW			
	ERBE-Like		SSF	
θ -range	Δ	RMS	Δ	RMS
$\theta < 50^\circ$	-2.73	3.12	0.03	1.42
$\theta < 70^\circ$	0.43	0.82	-0.06	0.51
	LW			
	ERBE-Like		SSF	
θ -range	Δ	RMS	Δ	RMS
$\theta < 50^\circ$	4.35	4.60	0.87	1.62
$\theta < 70^\circ$	1.22	1.33	0.29	0.49

Table 1 Mean regional SW and LW TOA flux bias (Δ) and *RMS* errors (W m^{-2}) for ERBE-Like and SSF TOA fluxes as a function of viewing zenith angle range.

Channel	All-Sky		Clear-Sky	
	ERBE-Like	SSF	ERBE-Like	SSF
SW	22.2 (37.5)	9.8 (12.5)	11.2	7.9
LW	5.8 (12.5)	3.5 (4.2)	3.7	2.4

Table 2 Estimated regional instantaneous SW and LW TOA flux errors in all-sky and clear-sky conditions. Numbers in parentheses correspond to values provided in Table 4 of Wielicki et al. (1995).

	SW Flux (W m ⁻²)		LW Flux (W m ⁻²)		SW CRF (W m ⁻²)		LW CRF (W m ⁻²)		Net CRF (W m ⁻²)		f (%)	τ (-)	Z _e (km)	Count (-)
	SSF	ES8	SSF	ES8	SSF	ES8	SSF	ES8	SSF	ES8				
Clear	40.5	38	286.5	288.4	-	-	-	-	-	-	-	-	-	-
Liquid	61.8	58.4	276.1	279.6	-21.3	-20.4	10.4	8.8	-10.9	-11.6	41	1.35	3.01	1925
Ice	118.8	111.9	211.2	216.7	-78.3	-73.9	75.3	71.7	-3	-2.2	85	2.36	8.84	1876
All	89.4	84.3	244.5	249	-48.9	-46.3	41.9	39.3	-7	-6.9	62	1.78	5.89	3839

Table 3 TOA fluxes and cloud radiative forcing in the west Pacific Ocean region (5°S-5°N, 140°E-165°E) for March 2000. ES8 corresponds to the ERBE-like result. Only daytime measurements are considered. “f” is cloud fraction; “ τ ” is cloud optical depth; “Z_e” is effective cloud height; “Count” is the number of 1° regions considered.

	SW Flux (W m ⁻²)		LW Flux (W m ⁻²)		SW CRF (W m ⁻²)		LW CRF (W m ⁻²)		Net CRF (W m ⁻²)		f (%)	τ (-)	Z _e (km)	Count (-)
	SSF	ES8	SSF	ES8	SSF	ES8	SSF	ES8	SSF	ES8				
Clear	40.1	36.3	282.2	283.9	-	-	-	-	-	-	-	-	-	-
Liquid	75.8	72.5	268.8	271.8	-35.7	-36.2	13.4	12.1	-22.3	-24.1	45	2.02	2.67	2798
Ice	124.5	120.2	219.8	223.8	-84.4	-83.9	62.4	60.1	-22.1	-23.8	73	3	7.87	914
All	84.7	81.3	258.4	261.5	-44.7	-45	23.8	22.3	-20.9	-22.6	49	2.23	3.95	3954

Table 4 Same as Table 3 but for east Pacific Ocean region (5°S-5°N, 80°W-105°W).

Model	Sensitivity Test
ADM	$(E, S, S) - (S, S, S)$
Clear-Sky Scene Identification	$(E, E, S) - (E, S, S)$
Directional Model	$(E, E, E) - (E, E, S)$
All	$(E, E, E) - (S, S, S)$

Table 5 Comparisons used to determine the TOA flux and cloud radiative forcing sensitivity to differences between SSF (S) and ERBE (E) ADMs (X), scene identification (Y) and directional models (Z).

	West Pacific Ocean Region														
	SW Flux (W m^{-2})			LW Flux (W m^{-2})			SW CRF (W m^{-2})			LW CRF (W m^{-2})			Net CRF (W m^{-2})		
	ES4	Non-GEO	GEO	ES4	Non-GEO	GEO	ES4	Non-GEO	GEO	ES4	Non-GEO	GEO	ES4	Non-GEO	GEO
Clear	40.6	40.7	40.7	290.8	290.3	289.3	-	-	-	-	-	-	-	-	-
All	82.5	83.1	81.9	262.7	261.2	261.7	-41.9	-42.4	-41.2	28.0	29.0	27.6	-13.9	-13.4	-13.6
	East Pacific Ocean Region														
	SW Flux (W m^{-2})			LW Flux (W m^{-2})			SW CRF (W m^{-2})			LW CRF (W m^{-2})			Net CRF (W m^{-2})		
	ES4	Non-GEO	GEO	ES4	Non-GEO	GEO	ES4	Non-GEO	GEO	ES4	Non-GEO	GEO	ES4	Non-GEO	GEO
Clear	39.4	41.2	41.2	283.16	281.5	279.8	-	-	-	-	-	-	-	-	-
All	120.1	115.1	115.4	221.20	223.5	222.9	-80.7	-73.8	-74.2	62.0	58.0	56.9	-18.7	-15.8	-17.3

Table 6 CRF (W m^{-2}) for March 1998 in the west and east Pacific Ocean regions as determined from the CERES SRBAVG and ERBE-Like (ES-4) products.

	West Pacific Ocean Region														
	SW Flux (W m^{-2})			LW Flux (W m^{-2})			SW CRF (W m^{-2})			LW CRF (W m^{-2})			Net CRF (W m^{-2})		
	ES4	Non-GEO	GEO	ES4	Non-GEO	GEO	ES4	Non-GEO	GEO	ES4	Non-GEO	GEO	ES4	Non-GEO	GEO
Clear	40.4	41.2	41.2	287.2	288.0	286.2	-	-	-	-	-	-	-	-	-
All	91.4	89.4	92.4	240.5	243.1	242.3	-51.0	-48.2	-51.2	46.7	44.9	43.8	-4.2	-3.3	-7.4
	East Pacific Ocean Region														
	SW Flux (W m^{-2})			LW Flux (W m^{-2})			SW CRF (W m^{-2})			LW CRF (W m^{-2})			Net CRF (W m^{-2})		
	ES4	Non-GEO	GEO	ES4	Non-GEO	GEO	ES4	Non-GEO	GEO	ES4	Non-GEO	GEO	ES4	Non-GEO	GEO
Clear	39.6	41.1	41.1	283.9	282.0	280.7	-	-	-	-	-	-	-	-	-
All	84.0	86.4	87.0	259.7	257.6	257.1	-44.4	-45.3	-45.9	24.2	24.4	23.6	-20.2	-20.9	-22.3

Table 7 Same as Table 6 but for March 2000.

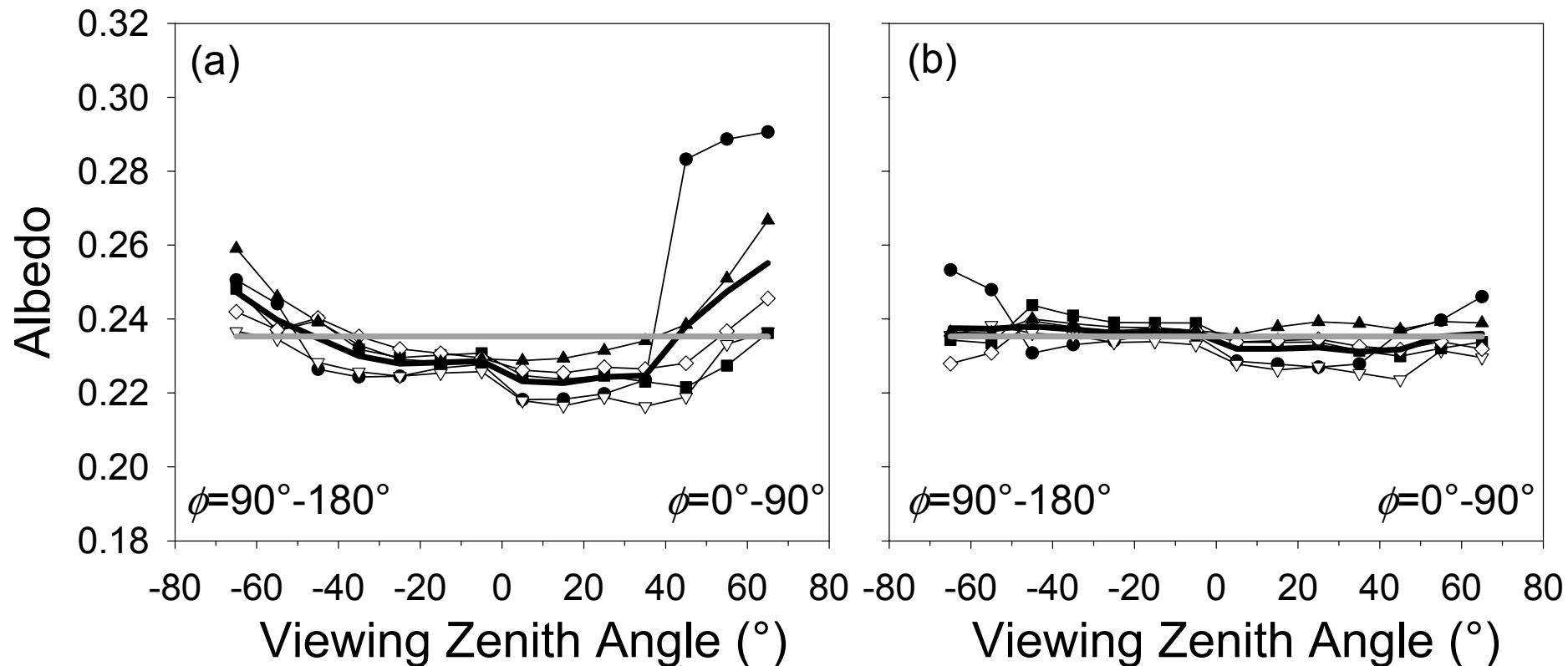


Figure 1

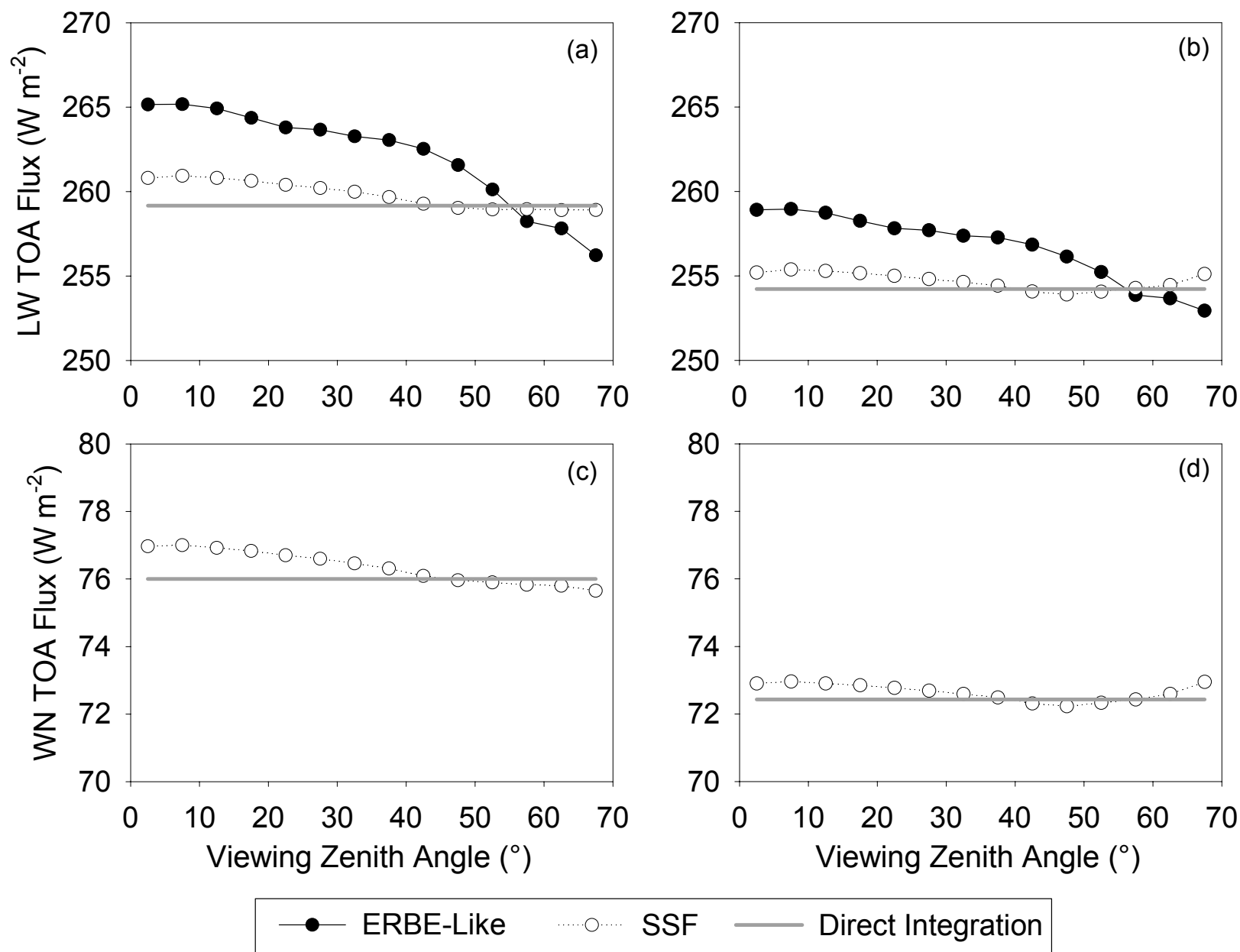


Figure 2

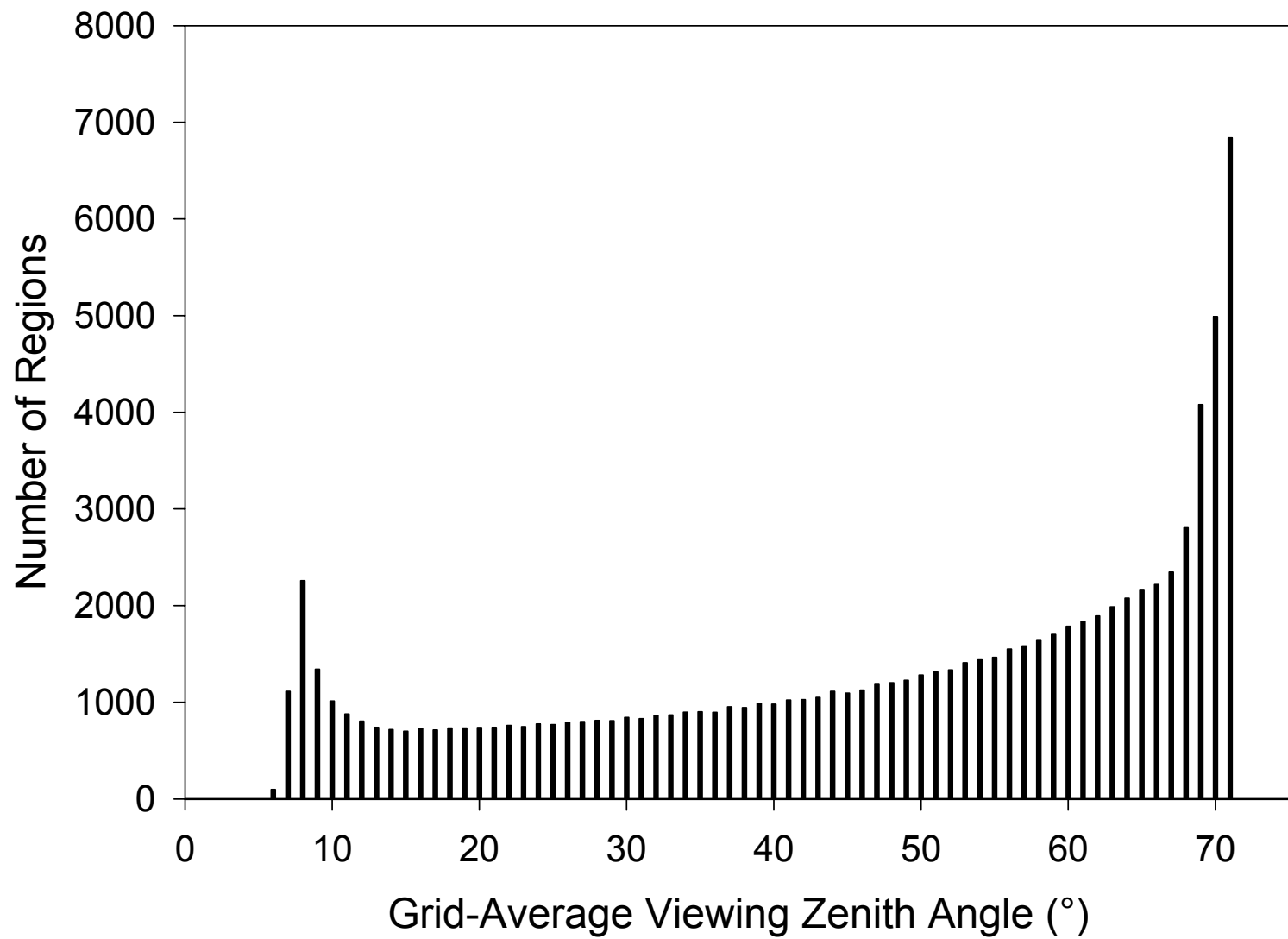


Figure 3

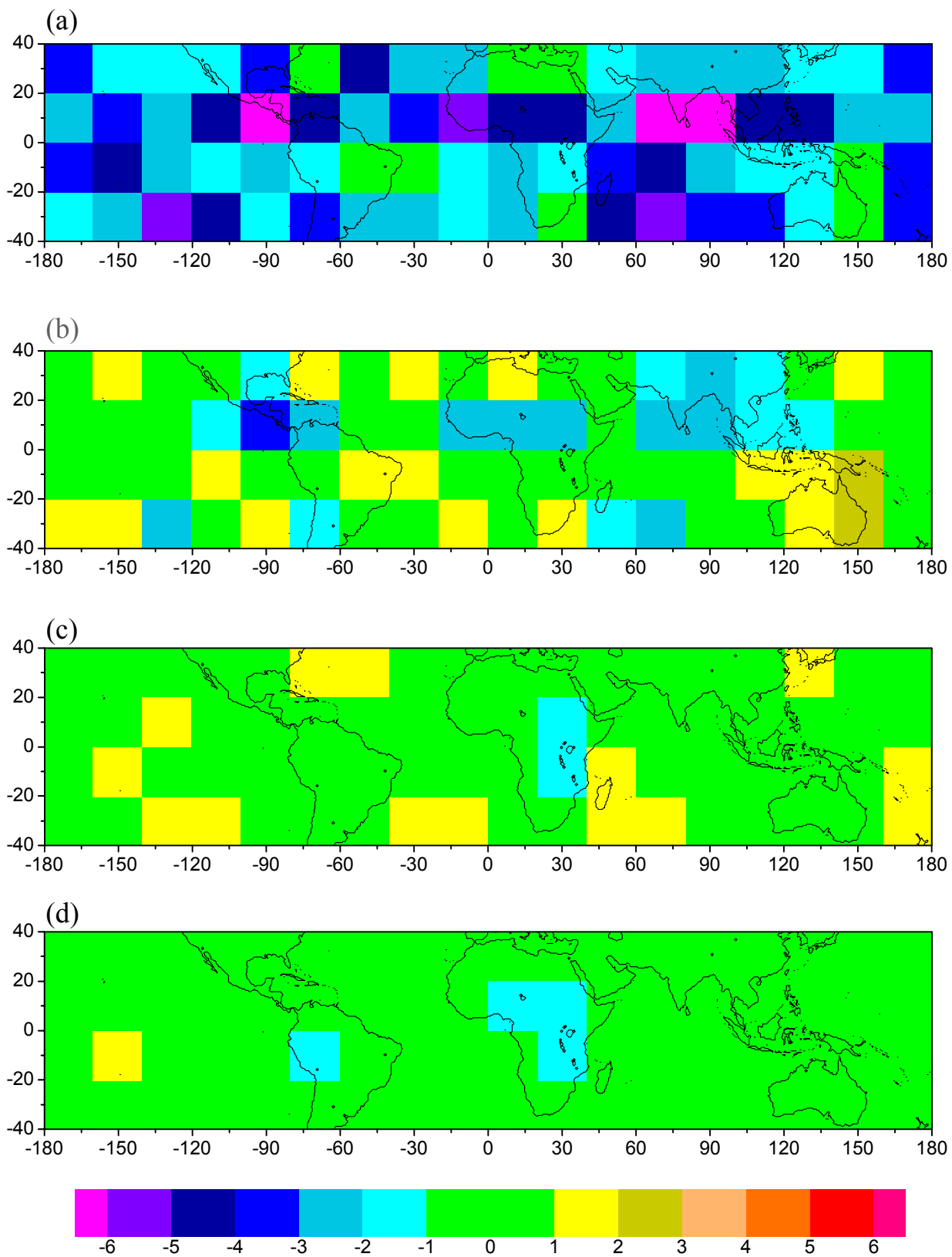


Figure 4

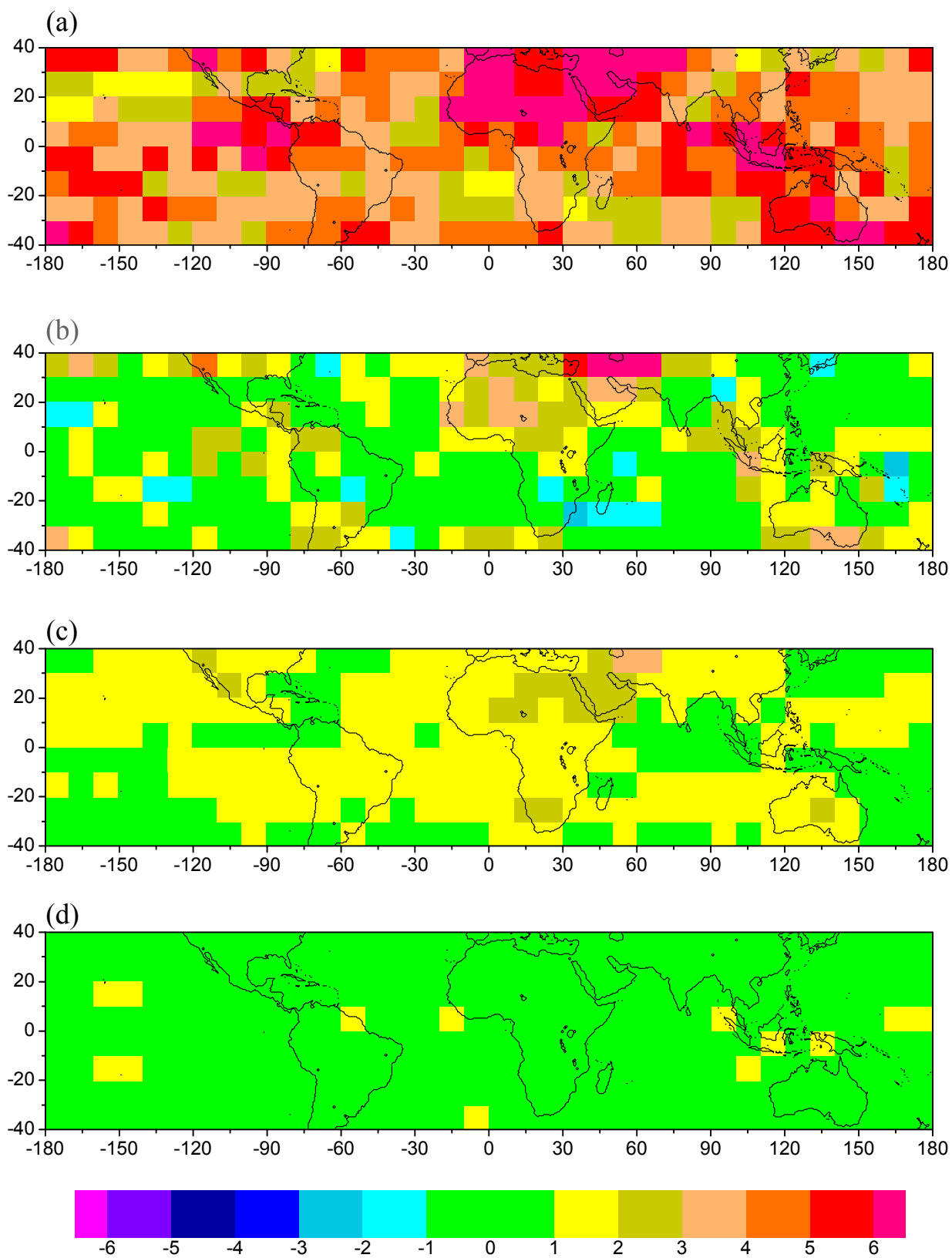


Figure 5

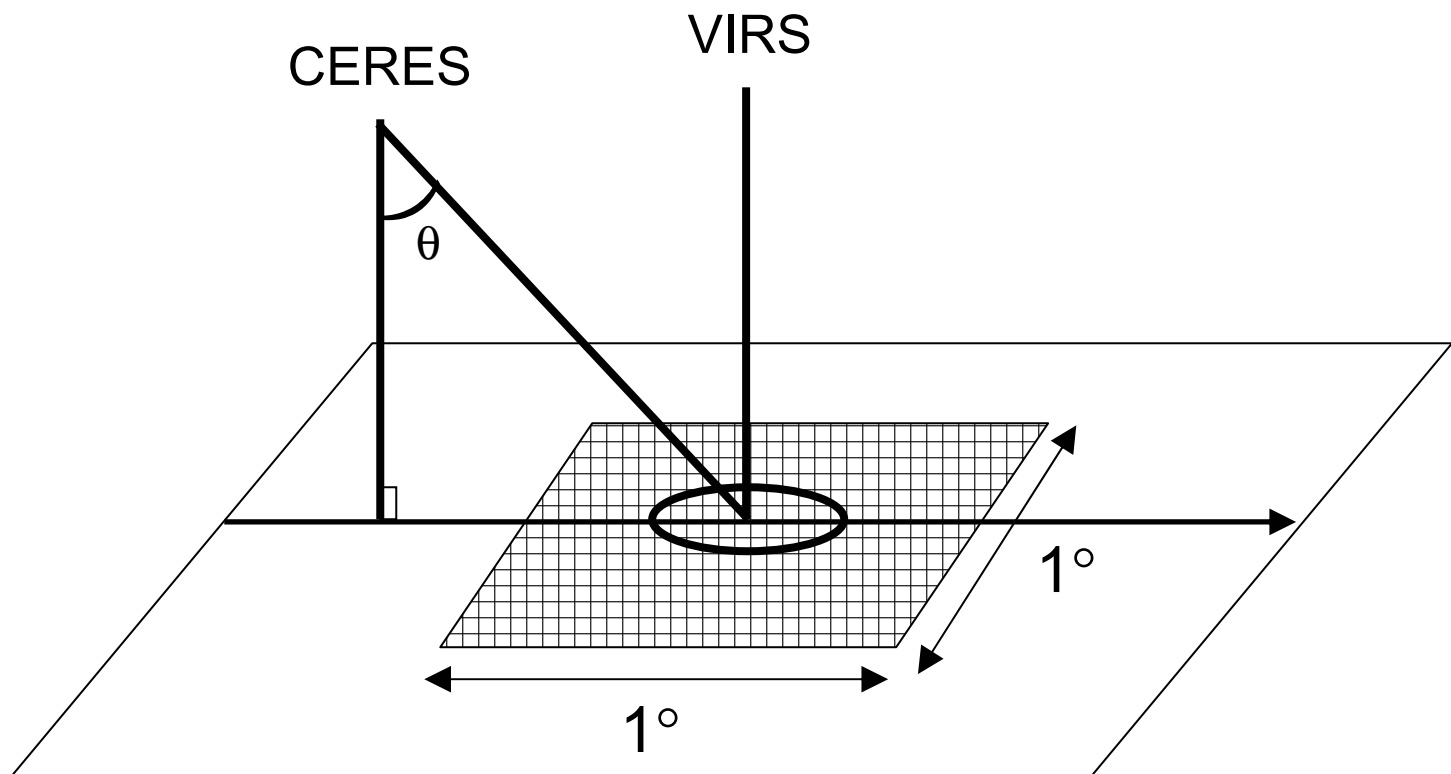


Figure 6

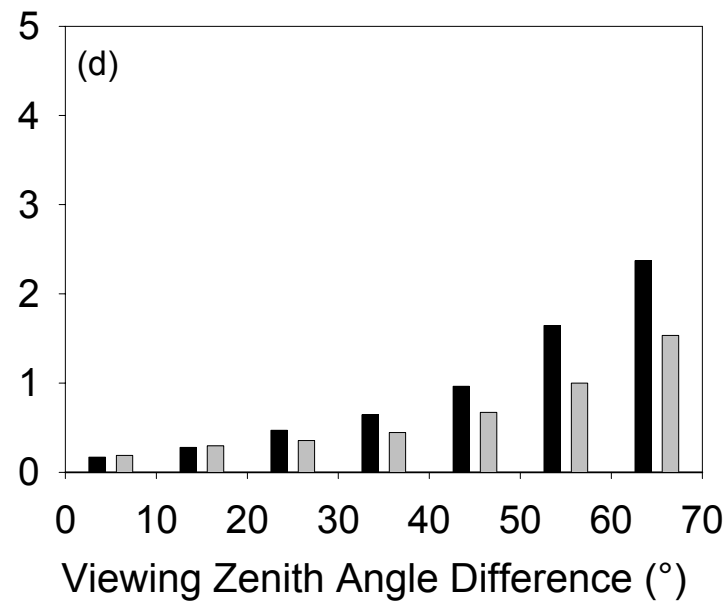
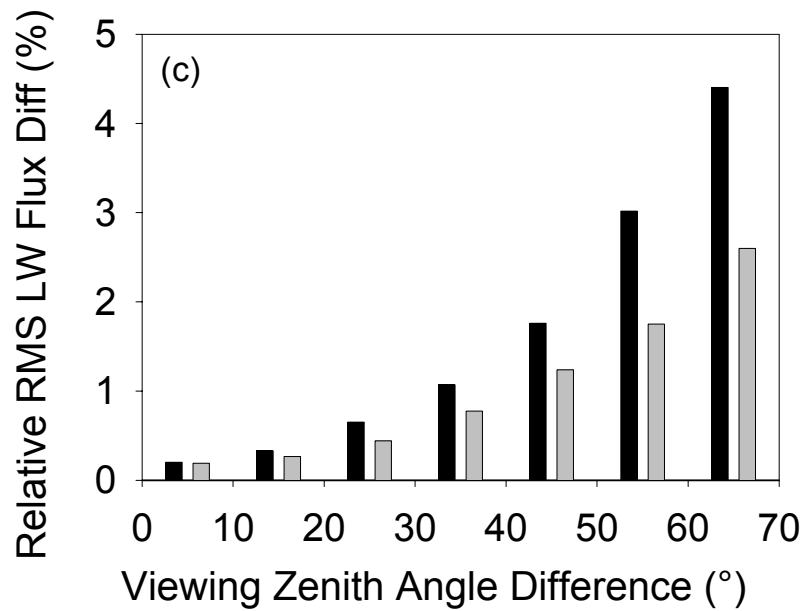
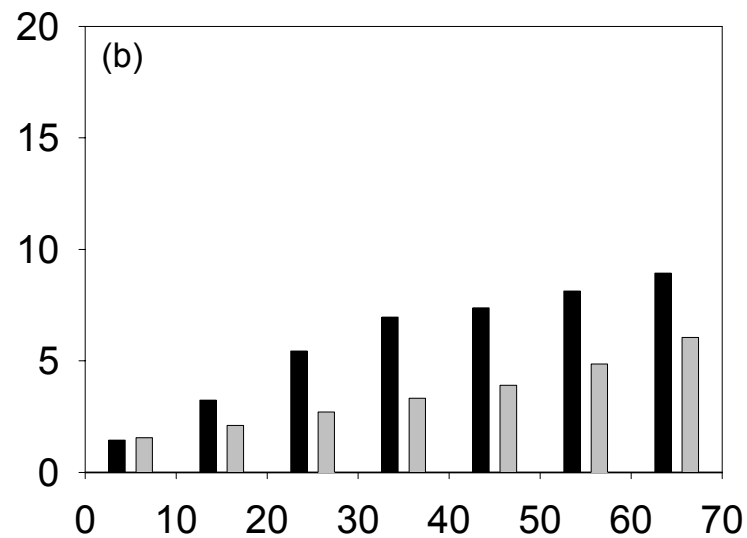
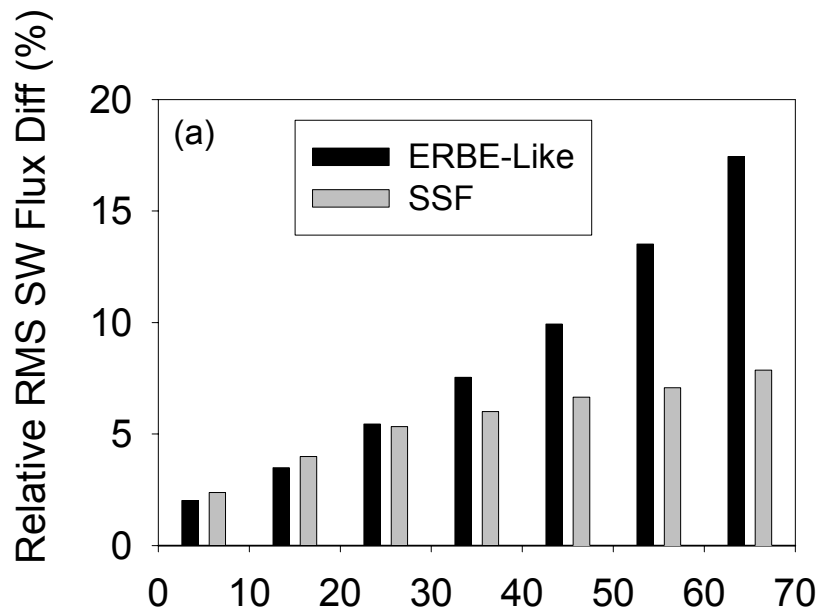


Figure 7

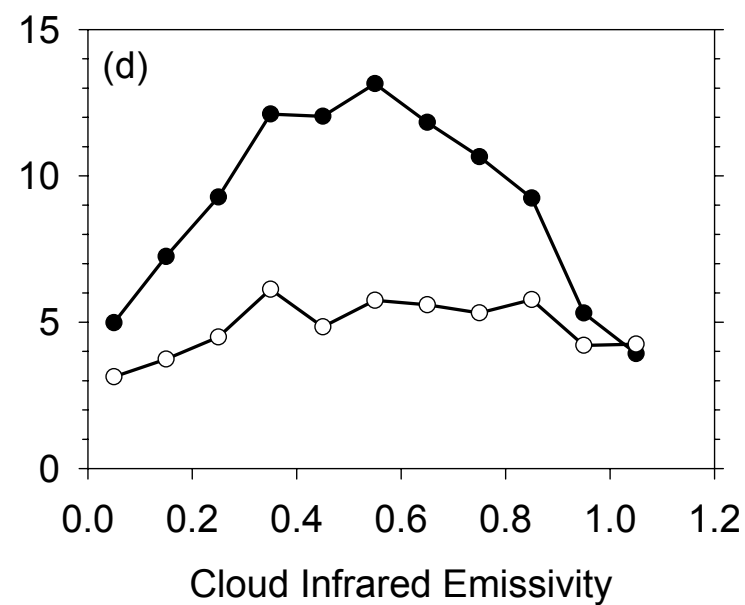
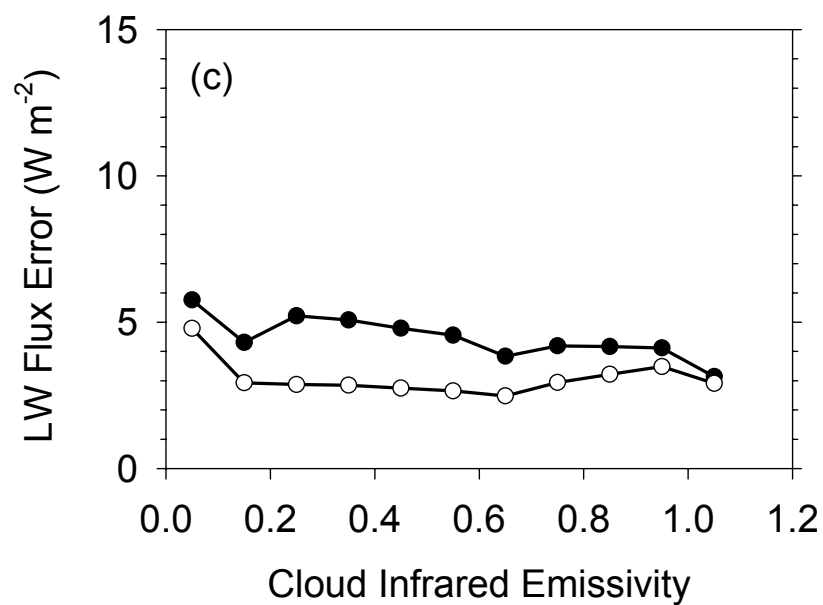
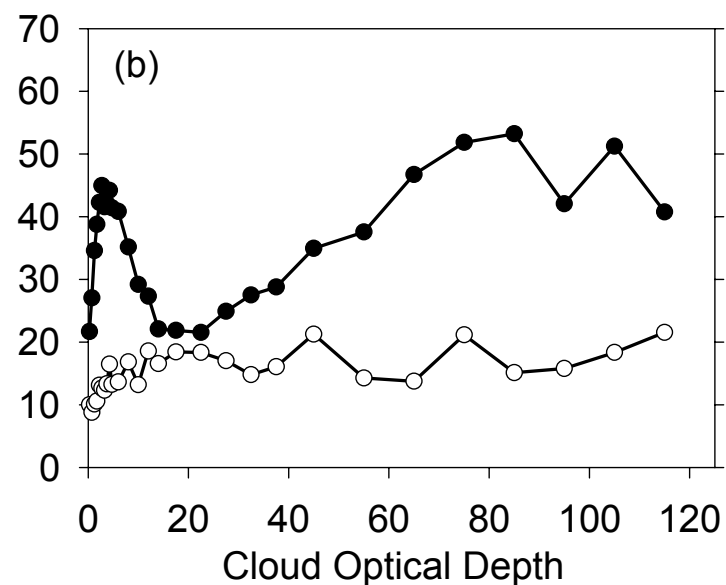
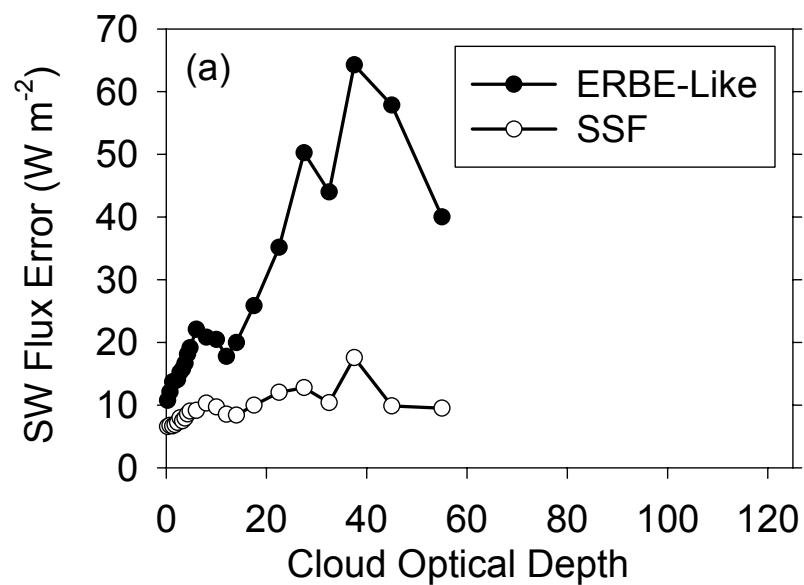


Figure 8

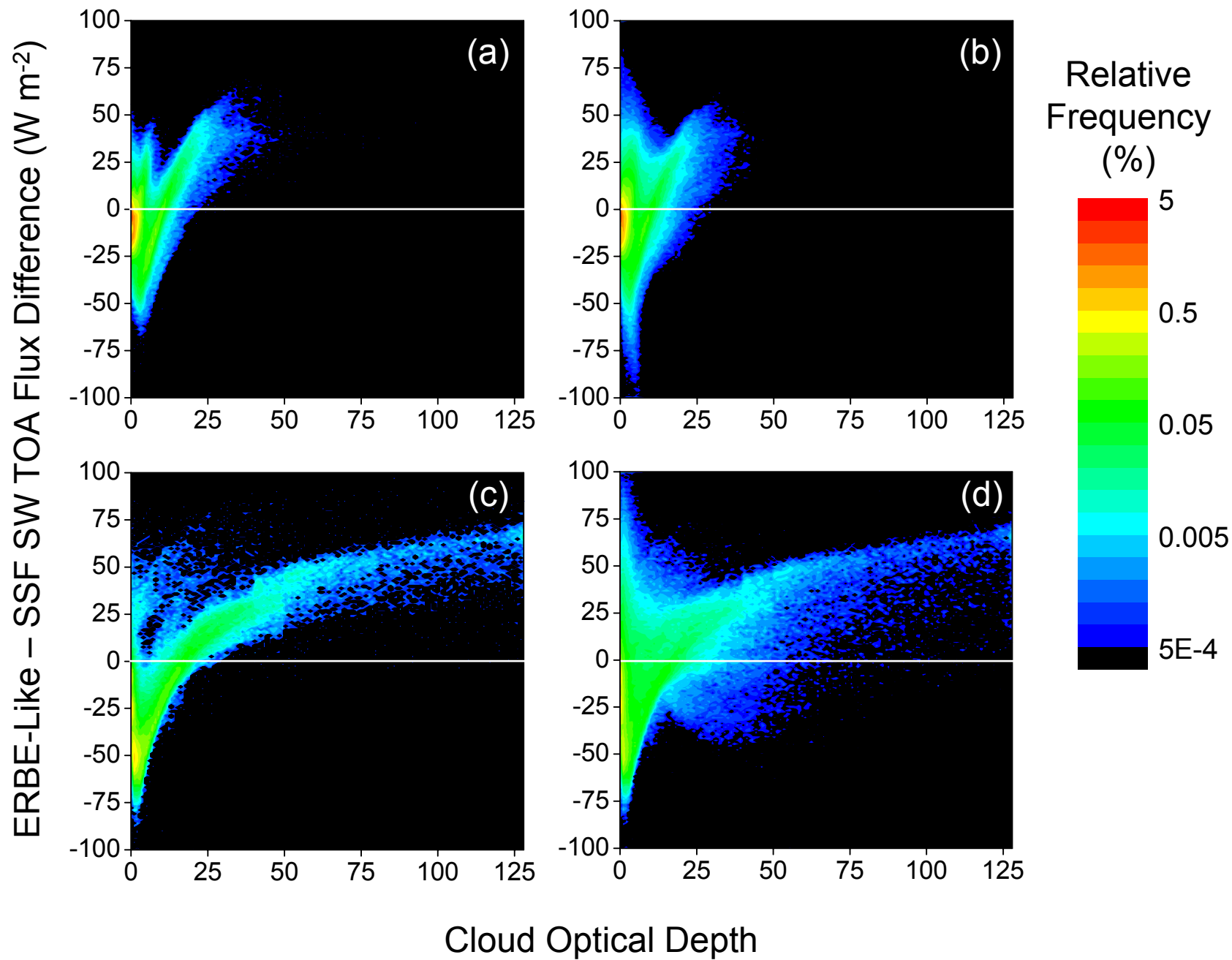


Figure 9

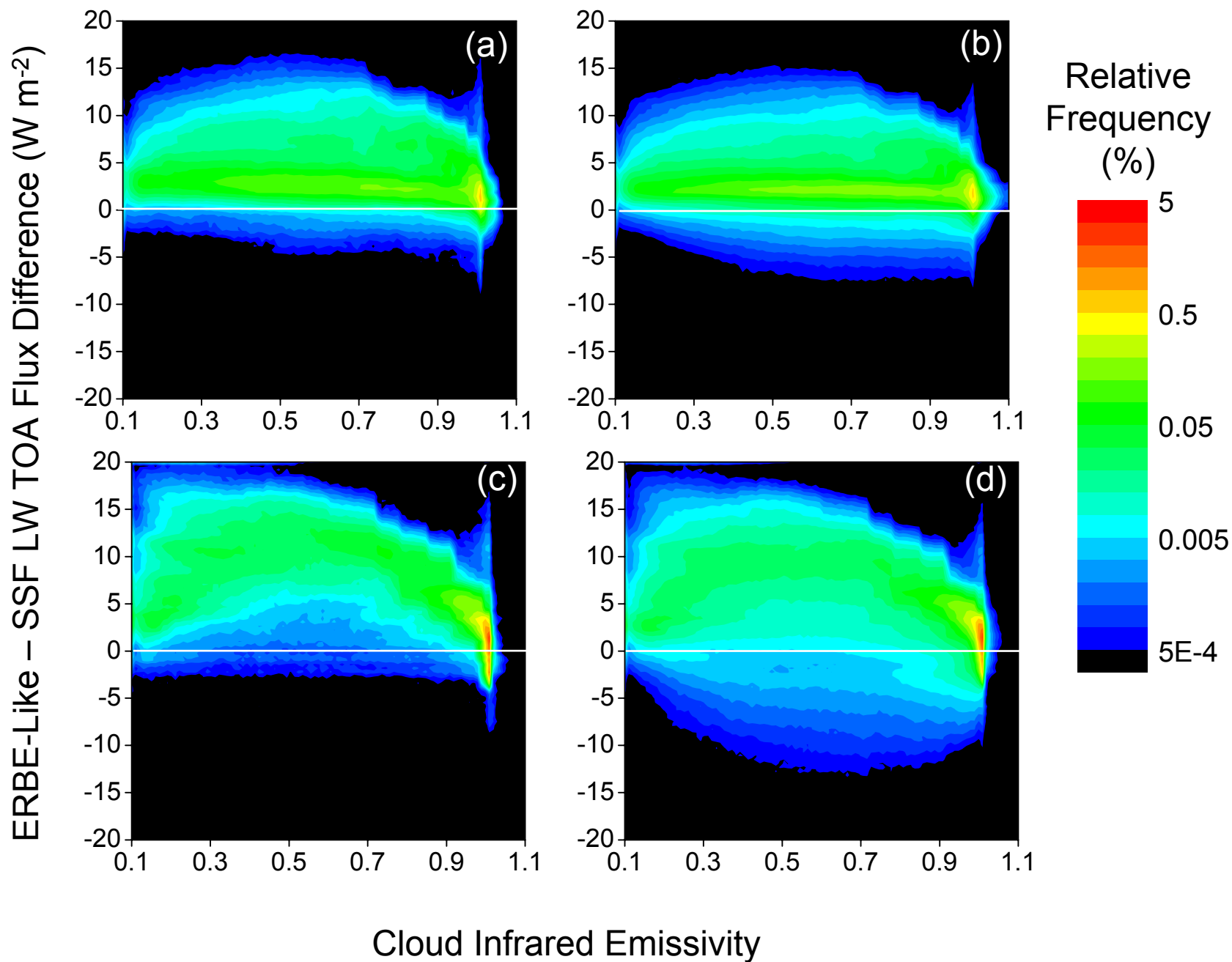


Figure 10

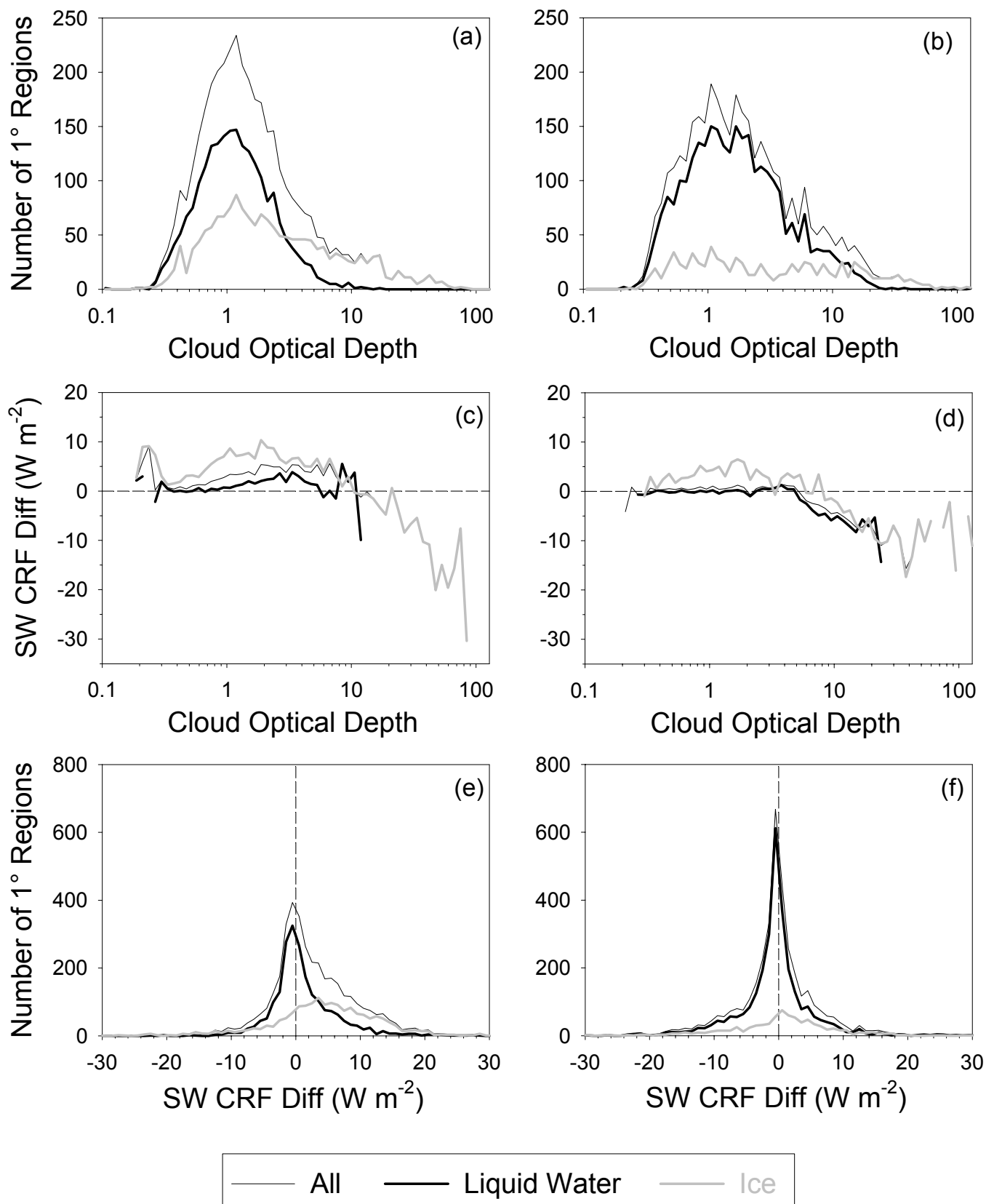


Figure 11

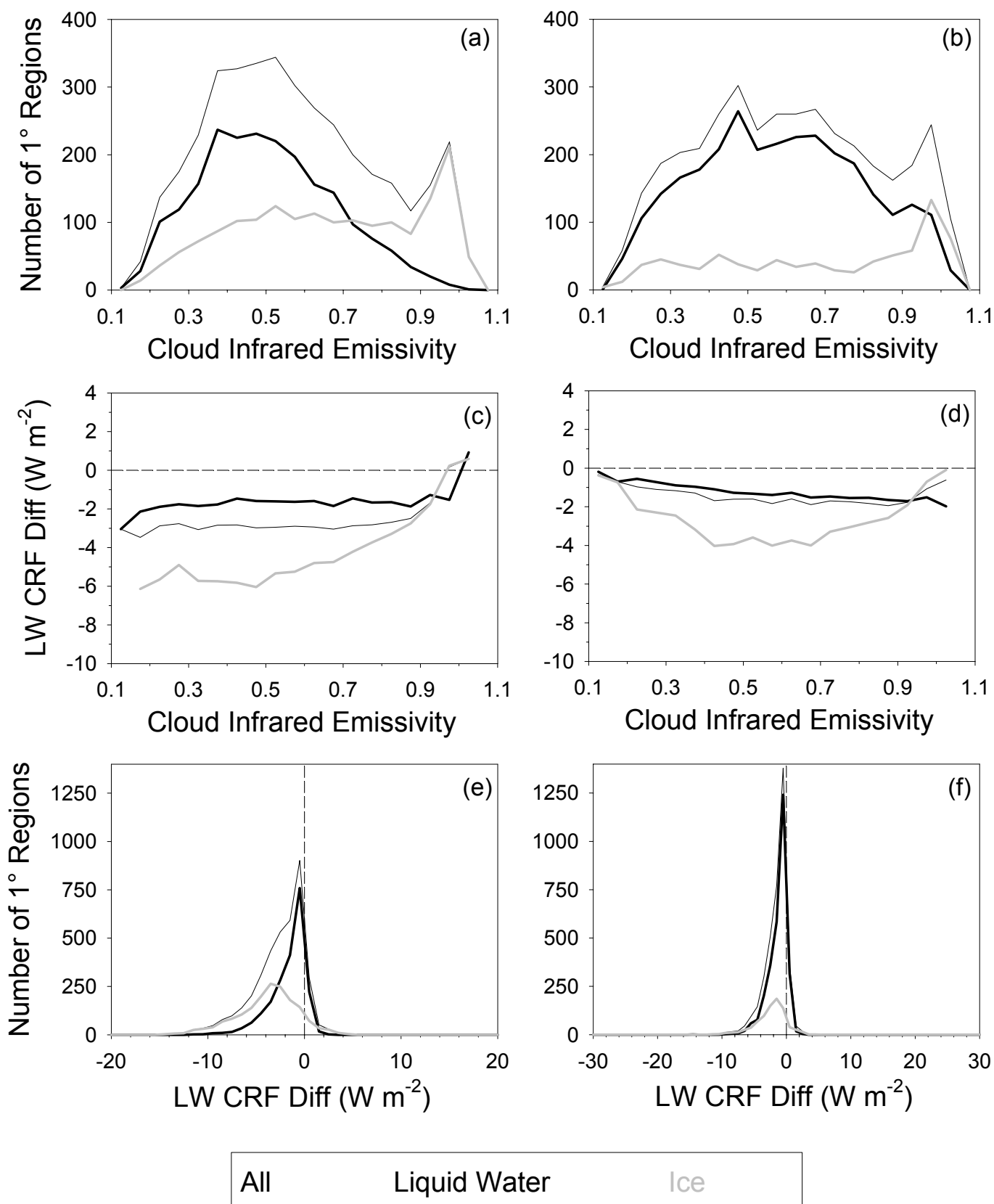


Figure 12

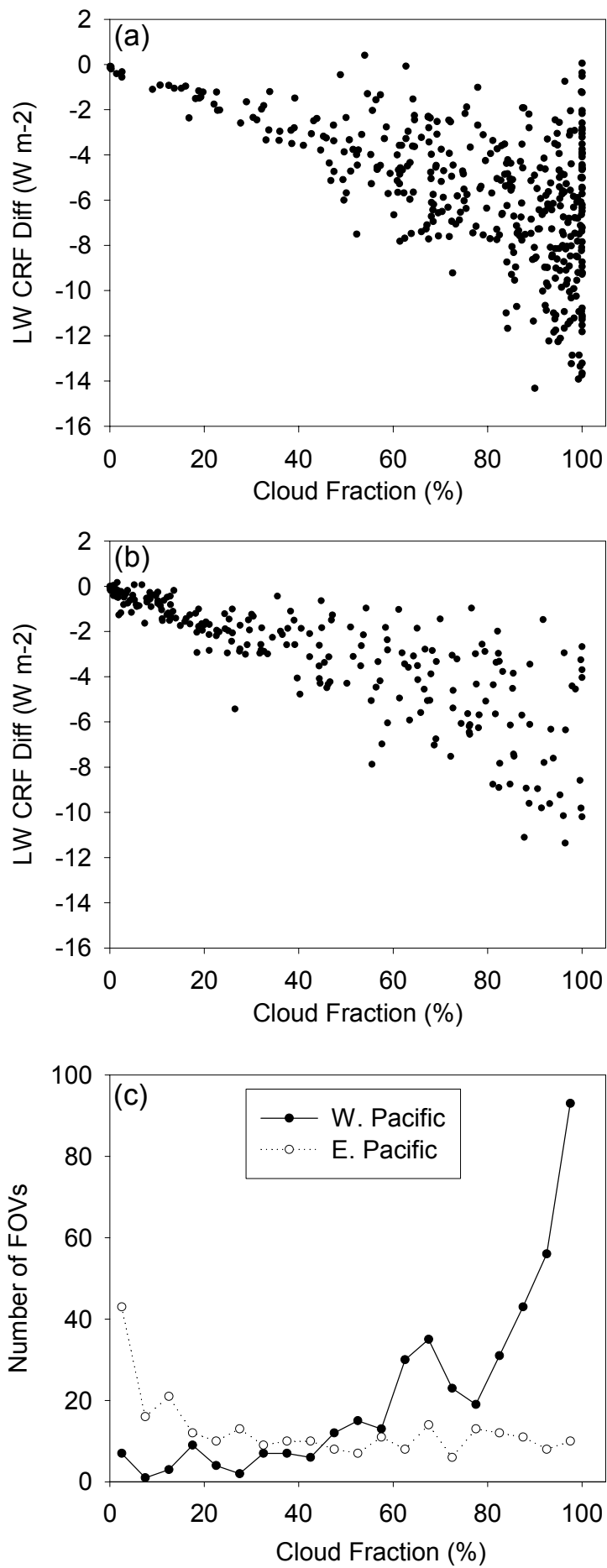


Figure 13

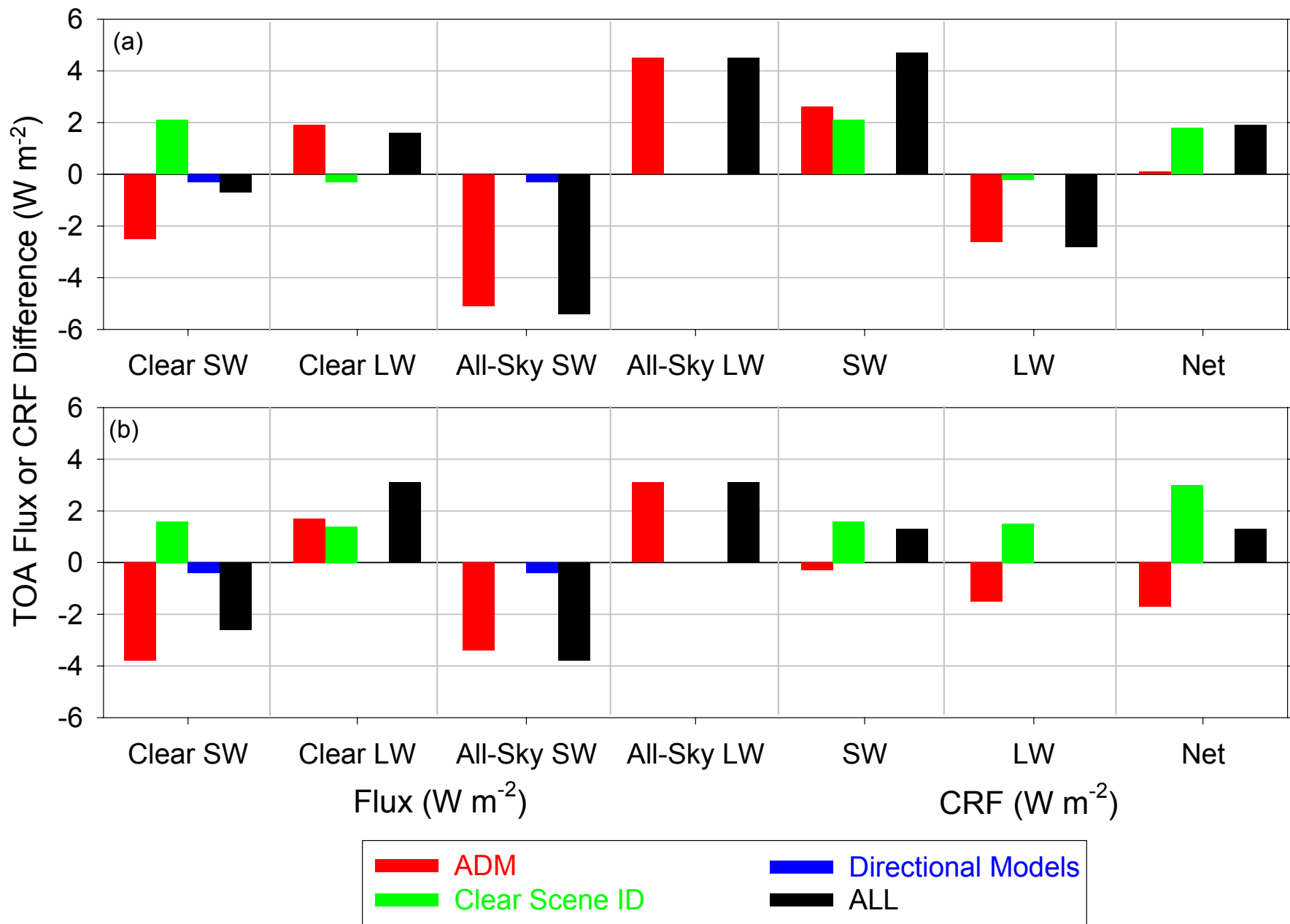


Figure 14

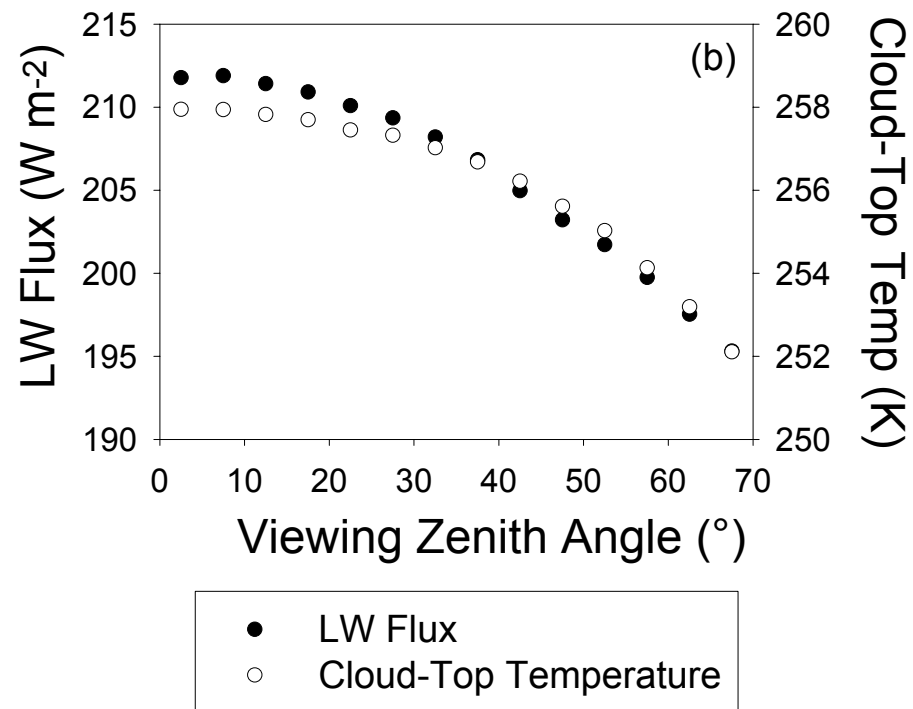
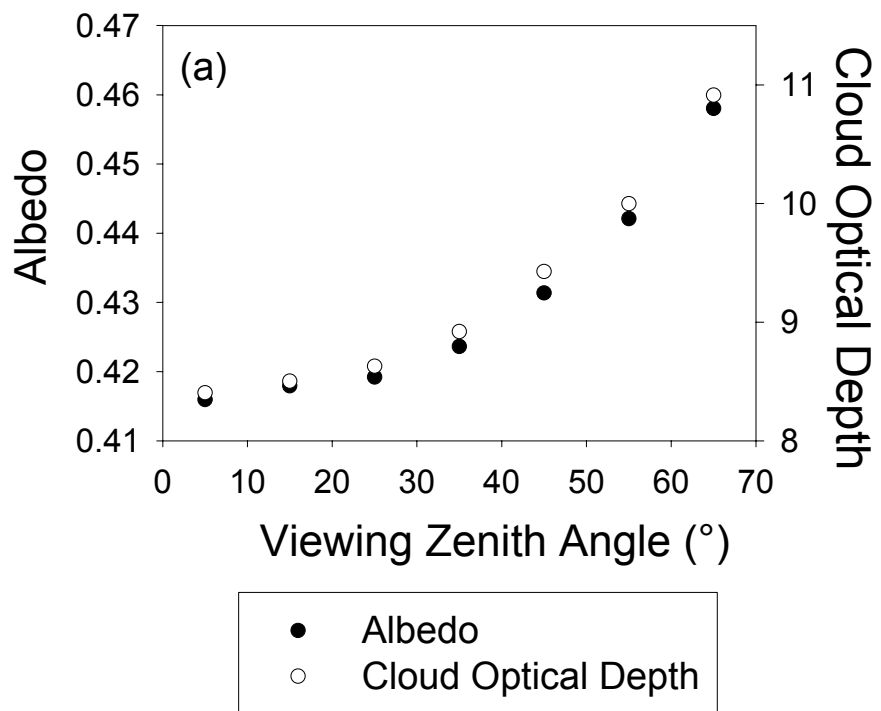


Figure 15